

1       **A Regional multi-Air Pollutant Assimilation System (RAPAS v1.0)**  
2               **for emission estimates: System development and application**

3       Shuzhuang Feng<sup>1</sup>, Fei Jiang<sup>1,2</sup>, Zheng Wu<sup>3</sup>, Hengmao Wang<sup>1,2</sup>, Wei He<sup>1</sup>, Yang Shen<sup>1</sup>,  
4               Lingyu Zhang<sup>1</sup>, Yanhua Zheng<sup>1</sup>, Chenxi Lou<sup>1</sup>, Ziqiang Jiang<sup>4</sup>, Weimin Ju<sup>1,2</sup>

5  
6       <sup>1</sup> *Jiangsu Provincial Key Laboratory of Geographic Information Science and Technology, International*  
7       *Institute for Earth System Science, Nanjing University, Nanjing, 210023, China*

8       <sup>2</sup> *Jiangsu Center for Collaborative Innovation in Geographical Information Resource Development and*  
9       *Application, Nanjing, 210023, China*

10      <sup>3</sup> *Chongqing Institute of Meteorological Sciences, Chongqing, 401147, China*

11      <sup>4</sup> *Jiangsu Environmental Monitoring Center, Nanjing, 210019, China*

12  
13  
14  
15  
16      *Correspondence to: Fei Jiang (jiangf@nju.edu.cn)*

30 **Abstract**

31 Top-down atmospheric inversion infers surface-atmosphere fluxes from spatially  
32 distributed observations of atmospheric compositions, which is a vital means for  
33 ~~quantifying~~ anthropogenic and natural emissions. In this study, we developed a  
34 Regional multi-Air Pollutant Assimilation System (RAPAS v1.0) based on the Weather  
35 Research and Forecasting/Community Multiscale Air Quality Modelling System  
36 (WRF/CMAQ) model, the three-dimensional variational (3DVAR) algorithm, and the  
37 ensemble square root filter (EnSRF) algorithm. This system can simultaneously  
38 assimilate hourly *in-situ* CO, SO<sub>2</sub>, NO<sub>2</sub>, PM<sub>2.5</sub> and PM<sub>10</sub> observations to infer gridded  
39 emissions of CO, SO<sub>2</sub>, NO<sub>x</sub>, primary PM<sub>2.5</sub> (PPM<sub>2.5</sub>), and coarse PM<sub>10</sub> (PMC) on a  
40 regional scale. In each data assimilation window, we use a “two-step” scheme, in which  
41 the emissions <sup>ARE</sup> ~~is~~ inferred first, and then input into the CMAQ model to simulate initial  
42 conditions (IC) of the next window. The posterior emissions ~~s~~ is transferred to the next  
43 window as the prior emission, and the original emission inventory is only used in the  
44 first window. Additionally, a “super-observation” approach is implemented to decrease  
45 the computational costs, observation error correlations, and influence of representative  
46 errors. Using this system, we estimated the emissions of CO, SO<sub>2</sub>, NO<sub>x</sub>, PPM<sub>2.5</sub>, and  
47 PMC in December and July 2016 over China using nationwide surface observations.  
48 The results showed ~~x~~ that compared to the prior emissions (MEIC 2016), the posterior  
49 emissions of CO, SO<sub>2</sub>, NO<sub>x</sub>, PPM<sub>2.5</sub>, and PMC in December 2016 increased by 129%,  
50 20%, 5%, 95%, and 1045%, respectively, and the emission uncertainties decreased by  
51 44%, 45%, 34%, 52%, and 56%, respectively. With the inverted emissions, the RMSE  
52 of simulated concentrations decreased by 40–56%. Sensitivity tests were conducted  
53 with different prior emissions, prior uncertainties, and observation errors. The results  
54 showed that the “two-step” scheme employed in RAPAS is robust in estimating  
55 emissions using nationwide surface observations over China. This study offers a useful  
56 tool for accurately quantifying multi-species anthropogenic emissions at large scales  
57 and in near real time.

s (Plural) → (singular)

in order to quantify

∅


∅ plural

present

58

59 **1. Introduction**

60 Owing to rapid economic development and pollution control legislation, there is an  
61 increasing demand to provide updated emission estimates, especially in areas where  
62 anthropogenic emissions are intensive. Accurately estimating source emission  
63 quantities and spatiotemporal changes resulting from various regulations is imperative  
64 and valuable for understanding air quality responses and is crucial for providing timely  
65 instructions for the design of future emission regulations. However, most inventories  
66 were developed based on a bottom-up approach and are usually updated with a delay  
67 of a few years owing to the complexity of gathering statistical information on activity  
68 levels and sector-specific emission factors (Ding et al., 2015). The large uncertainty  
69 associated with the low temporal and spatial resolutions of these datasets also greatly  
70 limits the assessment of emission changes. Some studies (Bauwens et al., 2020; Shi and  
71 Brasseur, 2020) evaluated emission changes indirectly through concentration  
72 measurements; however, air pollution changes are not only dominated by emission  
73 changes, but also highly affected by meteorological conditions (Shen et al., 2021).

74 Top-down atmospheric inversion infers surface-atmosphere fluxes from spatially  
75 distributed observations of atmospheric compositions. Recent efforts have <sup>been</sup> focused on   
76 developing air pollution data assimilation (DA) systems to conduct top-down  
77 inversions, which can integrate model and multi-source observational information to  
78 constrain emission sources. Two major methods are widely used in those DA systems:  
79 4D-variational data assimilation (4DVAR) and ensemble Kalman filter (EnKF).  
80 4DVAR provides a global optimal analysis by minimizing a cost function. It shows an  
81 implicit flow-dependent background error covariance and can reflect complex  
82 nonlinear constraint relationships (Lorenc, 2003). Additionally, a weak constraint  
83 4DVAR method can partly account for the model error by defining a systematic error  
84 term in a cost function (Derber, 1989). For example, the GEOS-Chem and TM5 4DVAR  
85 frameworks have been used to estimate CH<sub>4</sub> (Alexe et al., 2015; Monteil et al., 2013;  
86 Schneising et al., 2009; Stanevich et al., 2021; Wecht et al., 2014) and CO<sub>2</sub> fluxes (Basu  
87 et al., 2013; Nassar et al., 2011; Wang et al., 2019a) from different satellite retrieval

88 products. Additionally, Jiang et al. (2017) and Stavrou et al. (2008) also used the  
89 4DVAR algorithm to estimate global CO and NO<sub>x</sub> emission trends using MOPITT and  
90 GOME/SCIAMACHY retrievals, respectively. Using NIES LiDAR observations,  
91 Yumimoto et al. (2008) applied the 4DVAR DA to infer dust emissions over eastern  
92 Asia and the results agreed well with various satellite data and surface observations.  
93 Based on surface observations, Meirink et al. (2008) developed a 4DVAR system to  
94 optimize monthly methane emissions, which showed a high degree of consistency in  
95 posterior emissions and uncertainties when compared with an analogous inversion  
96 based on the traditional synthesis approach.

97 Although considerable progress has been made to reduce large uncertainties in emission  
98 inventories, the drawback of the 4DVAR method is the additional development of  
99 adjoint models, which are technically difficult and cumbersome for complex chemical  
100 transport models (Bocquet and Sakov, 2013). Instead, EnKF uses flow-dependent  
101 background error covariance generated by ensemble simulations to map deviations in  
102 concentrations to increments of emissions, which is more flexible and easier to  
103 implement. Many previous studies used EnKF techniques to assimilate single- or dual-  
104 species observations to optimize the corresponding emission species (Chen et al., 2019;  
105 Peng et al., 2017; Schwartz et al., 2014; Sekiyama et al., 2010). Miyazaki et al. (2017)  
106 improved NO<sub>x</sub> emission estimates using multi-constituent satellite observations, and  
107 further estimated global surface NO<sub>x</sub> emissions from 2005 to 2014. Feng et al., (2020b)  
108 used surface observations of NO<sub>2</sub> to infer the NO<sub>x</sub> emission changes in China during  
109 the COVID-19, and quantitatively evaluate the impact of the epidemic on economic  
110 activities from the perspective of emission change. Tang et al. (2011) adjusted the  
111 emissions of NO<sub>x</sub> and VOCs through assimilating surface O<sub>3</sub> observations and achieved  
112 an better performance in O<sub>3</sub> forecasts. However, such a revision may encounter the  
113 problem of model error compensation rather than a retrieval of physically meaningful  
114 quantities, which should be avoided from overfitting for emission inversion purposes  
115 (Bocquet, 2012; Navon, 1998; Tang et al., 2011). The EnKF has also been widely  
116 applied to optimize emissions of carbon dioxide (Jiang et al., 2021; Liu et al., 2019),

117 carbon monoxide (Feng et al., 2020a; Mizzi et al., 2018), sulfur dioxide (Chen et al.,  
118 2019), ammonia (Kong et al., 2019), etc.

119 Multi-species data assimilation can efficiently reduce the uncertainty in emission  
120 inventories and has led to improvements in air quality forecasting (Ma et al., 2019;  
121 Miyazaki et al., 2012b) as it offers additional constraints on emission estimates through  
122 improvements in related atmospheric fields, chemical reactions, and gas-particle  
123 transformations (Miyazaki and Eskes, 2013). Barbu et al. (2009) updated sulfur oxide  
124 ( $\text{SO}_x$ ) emissions with  $\text{SO}_2$  and sulfate aerosol observations and found that the  
125 simultaneous assimilation of both species performed better than assimilating them  
126 separately. Muller and Stavrou (2005) also found that the simultaneous optimization  
127 of the sources of CO and  $\text{NO}_x$  led to better agreement between simulations and  
128 observations compared to the case where only CO observations are used.

129 The deviation in the chemical initial conditions (IC) is an important source of error that  
130 affects the accuracy of emission inversion because atmospheric inversion fully  
131 attributes the biases in simulated and observed concentrations to deviations in  
132 emissions (Meirink et al., 2006; Peylin et al., 2005). The biases of concentrations would  
133 be compensated by the unreasonable adjustment of pollution emissions without the  
134 optimization of ICs (Tang et al., 2013). Simultaneously optimizing chemical ICs and  
135 emissions has been applied to constrain emissions in many previous studies (Ma et al.,  
136 2019; Miyazaki et al., 2012a; Peng et al., 2018). For example, Elbern et al. (2007)  
137 adjusted  $\text{O}_3$  ICs,  $\text{NO}_x$  ICs and emissions, VOCs ICs and emissions jointly through  
138 assimilating surface  $\text{O}_3$  and  $\text{NO}_x$  observations. Although the forecast skills of  $\text{O}_3$  were  
139 improved, due to the coarse model resolution and the strong nonlinear relationship  
140 between  $\text{O}_3$  and  $\text{NO}_x$ , the assimilation of  $\text{O}_3$  observation worsened emission inversion  
141 and forecast of  $\text{NO}_x$ . Peng et al. (2018) assimilated near-surface observations to  
142 simultaneously optimize the ICs and emissions. In the 72-hr forecast evaluation, their  
143 resultant emission succeeded in improving  $\text{SO}_2$  forecast while having little influence  
144 on CO and aerosol forecast and even degrading the forecast of  $\text{NO}_2$ . Ma et al. (2019)  
145 also found that the DA benefits for forecast almost disappeared after 72 hr using

unclear

Optimal  
 $\text{O}_3$ ,  $\text{NO}_x$  and VOC ICs  
AND  
 $\text{NO}_x$  and VOCs emissions

146 optimized ICs and emissions. Although a large improvement has been achieved, this  
147 method has significant limitations in emission inversion as the contributions from the  
148 emissions and chemical ICs to the model's biases are difficult to distinguish (Jiang et  
149 al., 2017). In addition, the constraints of the chemical ICs with observations in each  
150 assimilation window make the emission inversions between the windows independent.  
151 This means that if the emission in one window is overestimated or underestimated, it  
152 cannot be transferred to the next window for further correction and compensation.  
153 Considering the importance of emissions in chemical field prediction (Bocquet et al.,  
154 2015), the rapid disappearance of the DA benefits seems unrealistic, indicating that  
155 simultaneously optimizing chemical ICs and emissions may result in a systematic bias  
156 in the inverted emissions (Jiang et al., 2021).

157 Since 2013, China has deployed an air pollution monitoring network that publishes  
158 nationwide and real-time hourly surface observations. This dataset provides an  
159 opportunity to improve emission estimates using the DA. In this study, a regional multi-  
160 air pollutant assimilation system using 3DVAR and EnKF DA techniques was  
161 constructed to simultaneously assimilate various surface observations (e.g. CO, SO<sub>2</sub>,  
162 NO<sub>2</sub>, O<sub>3</sub>, PM<sub>2.5</sub>, and PM<sub>10</sub>). We adopted a “two-step” method in this system, in which  
163 the ICs of each DA window were simulated using the posterior emissions of the  
164 previous DA window. The capabilities of RAPAS for reanalysis field generation and  
165 emission inversion estimation were also evaluated. The robustness of the system was  
166 investigated with different prior inventories, uncertainty settings of prior emissions, and  
167 observation errors. The remainder of the paper is organized as follows: Section 2  
168 introduces the DA system and observation data, Section 3 describes the experimental  
169 design, Section 4 presents and discusses the results of the system performance and  
170 sensitivity tests, and Section 5 concludes the paper.

## 171 **2. Method and data**

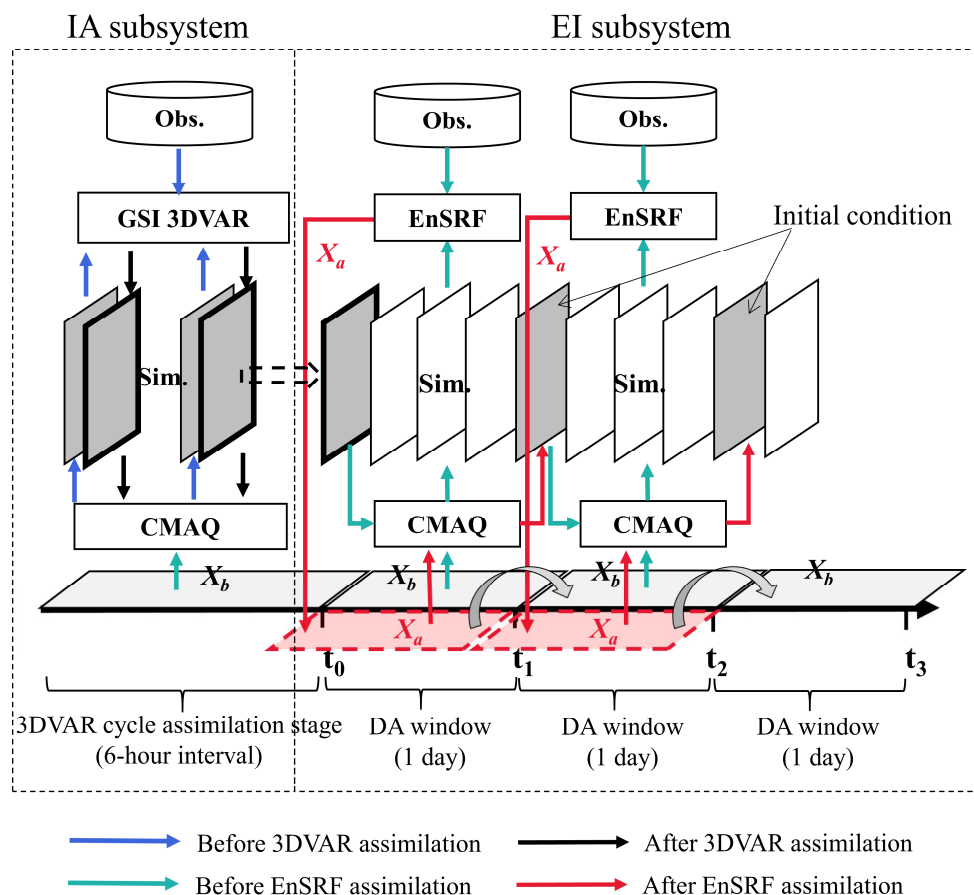
### 172 **2.1 System description**

#### 173 **2.1.1 Procedure of the assimilation system**

174 A regional air pollutant assimilation system has been preliminarily constructed and  
175 successfully applied in our previous studies to optimize the gridded CO and NO<sub>x</sub>  
176 emissions (Feng et al., 2020a; Feng et al., 2020b). Herein, the system was further  
177 extended to simultaneously assimilate multiple species (e.g. CO, SO<sub>2</sub>, NO<sub>2</sub>, O<sub>3</sub>, PM<sub>2.5</sub>,  
178 and PM<sub>10</sub>) and officially named the Regional multi- Air Pollutant Assimilation System  
179 (RAPASv1.0). The RAPAS has three components: a regional chemical transport model  
180 (CTM), which is coupled offline and used to simulate the meteorological fields and  
181 atmospheric compositions, and the 3DVAR and ensemble square root filter (EnSRF)  
182 modules, which are used to optimize chemical ICs (Feng et al., 2018; Jiang et al., 2013b)  
183 and anthropogenic emissions (Feng et al., 2020a; Feng et al., 2020b), respectively.  
184 3DVAR was introduced considering its excellent performance in our previous study and  
185 the lower computational cost during the spin-up period in optimizing ICs. Additionally,  
186 the 3DVAR method can obtain a better IC than the EnKF method (Schwartz et al., 2014).

187 Based on the above three components, the RAPAS was divided into two subsystems:  
188 the IC assimilation (IA) subsystem (CTM plus 3DVAR) and the emission inversion (EI)  
189 subsystem (CTM plus EnSRF). As shown in Figure 1, the IA subsystem was first run  
190 to optimize the chemical ICs (Kleist et al., 2009; Wu et al., 2002) for the subsequent EI  
191 subsystem. Distinguish the source type of model-observation mismatch error was not  
192 required for the IA subsystem. The EI subsystem runs cyclically with a “two-step”  
193 scheme. In the first step, the prior emissions ( $X^b$ ) are perturbed and input into the CTM  
194 model to simulate chemical concentration ensembles. The simulated concentrations of  
195 the lowest model level were then interpolated to the observation space according to the  
196 locations and times of the observations using the nearest-neighbor interpolation method.  
197 Prior emissions ( $X^b$ ), simulated observations and real observations were entered into  
198 the EnSRF module to generate optimized emissions ( $X^a$ ). In the second step, the  
199 optimized emissions were re-entered into the CTM model to generate the ICs of the  
200 next DA window. Meanwhile, the optimized emissions were transferred to the next  
201 window as prior emissions. Unlike joint adjustment of ICs and emissions (“one-step”  
202 scheme) in emission inversion (Chen et al., 2019), the “two-step” scheme needs to run

203 the CTM model twice, which is time consuming but can transfer the potential errors of  
 204 the inverted emissions in one DA window to the next for further correction.



205

206 **Figure 1.** Composition and flow chart of RAPAS.  $x_a$  and  $x_b$  represent the prior and  
 207 posterior emissions. The 3DVAR assimilation stage lasts five days with data input  
 208 frequency of six hours and the DA window in the EI subsystem is set to one day.

209 **2.1.2 Atmospheric transport model**

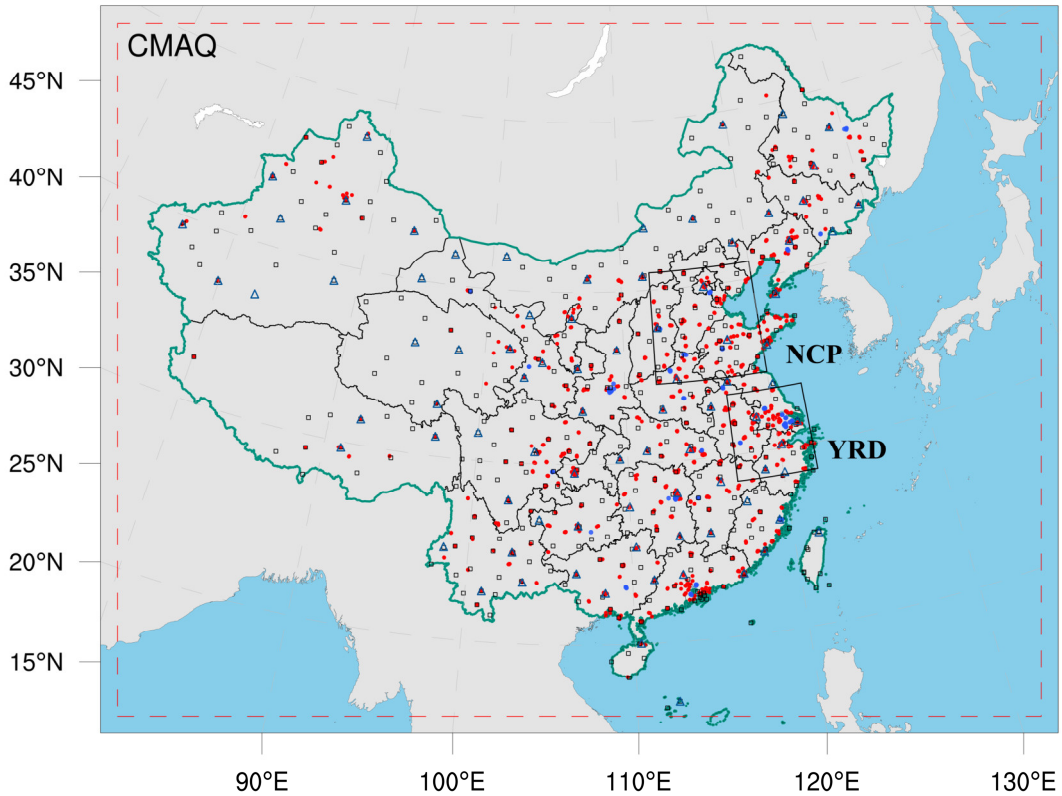
210 The regional chemical transport model of <sup>the</sup> Weather Research and  
 211 Forecasting/Community Multiscale Air Quality Modelling System (WRF/CMAQ) was  
 212 adopted in this study. CMAQ is a regional 3-D Eulerian atmospheric chemistry and  
 213 transport model with a “one-atmosphere” design developed by the US Environmental  
 214 Protection Agency (EPA). It can simultaneously address the complex interactions  
 215 among multiple pollutants/air quality issues. The CMAQ <sup>model</sup> was driven by the WRF model,  
 216 which is a state-of-the-art mesoscale numerical weather prediction system designed for

*of "CMAQ was..."*



217 both atmospheric research and meteorological field forecasting. In this study, WRF  
218 version 4.0 and CMAQ version 5.0.2 were used. The WRF simulations were performed  
219 with a 36-km horizontal resolution on  $169 \times 129$  grids, covering all of mainland China  
220 (Figure 2). This spatial resolution has been widely adopted in regional simulations as it  
221 can provide good simulations of spatiotemporal variations in air pollutants (Mueller  
222 and Mallard, 2011; Sharma et al. 2016). In the vertical direction, there were 51 sigma  
223 levels on the sigma-pressure coordinates extending from the surface to 100 hPa. The  
224 underlying surface of the urban and built-up land was replaced by the MODIS land  
225 cover retrieval of 2016 to adapt to the rapid expansion of urbanization. The CMAQ  
226 model was run with the same domain but with three grid cells removed from each side  
227 of the WRF domain. There were 15 layers in the CMAQ vertical coordinates, which  
228 were interpolated from 51 WRF layers.

229 The meteorological initial and lateral boundary conditions were both provided by the  
230 Final Operational Global Analysis data of the National Center for Environmental  
231 Prediction (NCEP) with a  $1^\circ \times 1^\circ$  resolution at 6-h intervals. The chemical lateral  
232 boundary conditions and chemical ICs in the IA subsystem originate from background  
233 profiles. As mentioned above, in the EI subsystem, the chemical IC in the first window  
234 is provided by the IA subsystem and in the following windows, it is forward simulated  
235 using optimized emissions from the previous window. Carbon Bond 05 with updated  
236 toluene chemistry (CB05tucl) and the 6th generation aerosol module (AERO6) were  
237 chosen as the gas-phase and aerosol chemical mechanisms, respectively (Appel et al.,  
238 2013; Sarwar et al., 2012). The detailed physical and chemical configurations are listed  
239 in Table 1.



240

241 **Figure 2.** Model domain and observation network. The red dashed frame depicts the  
 242 CMAQ computational domain; the black squares represent the surface meteorological  
 243 measurement sites; the navy <sup>blue</sup> triangles represent the sounding sites; and the red and blue  
 244 dots represent the air pollution measurement sites. Observations from all sites were  
 245 assimilated in the 3DVAR subsystem, while observations of city sites where red dots  
 246 were averaged are used for assimilation and where blue dots were averaged are used  
 247 for independent evaluation in the EI subsystem; the boxed subregions are the North  
 248 China Plain (NCP) and Yangtze River Delta (YRD); and the shaded area depicts the  
 249 topography.

250

251

252

253

254

255 **Table 1.** Configuration options of WRF/CMAQ

WRF		CMAQ	
Parameter	Scheme	Parameter	Scheme
Microphysics	WSM6	Horizontal/Vertical advection	yamo/wrf
Longwave	RRTM	Horizontal/Vertical diffusion	multiscale/acm2
Shortwave	Goddard	Deposition	m3dry
Boundary layer	ACM	Chemistry solver	EBI
Cumulus	Kain-Fritsch	Photolysis	phot_inline
Land-surface	Noah	Aerosol module	AERO6
Surface layer	Revised	Cloud module	cloud_acm_ae6
Urban canopy	No	Gas-phase chemistry	CB05tucl

256 **2.1.3 3DVAR assimilation algorithm**

257 Grid-point Statistical Interpolation (GSI) developed by the US NCEP was utilized in  
 258 this study. Building on the work of Liu et al. (2011), Jiang et al. (2013b) and Feng et al.  
 259 (2018), we extended GSI to simultaneously assimilate multiple species (including CO,  
 260 SO<sub>2</sub>, NO<sub>2</sub>, O<sub>3</sub>, PM<sub>2.5</sub>, and PM<sub>10</sub>) and first used individual aerosol species of PM<sub>2.5</sub> as  
 261 analysis variables within the GSI/WRF/CMAQ framework. Additional work includes  
 262 the construction of surface air pollutant observation operators, the updating of  
 263 observation errors, and the statistics of background error covariance for the analysis  
 264 variables. Moreover, the data interface was modified to read/write the CMAQ  
 265 output/input file directly, which was easy to implement.

266 In the sense of minimum analysis error variance, the 3DVAR algorithm optimizes the  
 267 analysis fields with observations by <sup>van</sup> iterative processes to minimize the cost function  
 268 ~~J(x)~~ defined below: *remove extra parenthesis*

$$269 \quad J(x) = \frac{1}{2}(\mathbf{x}_a - \mathbf{x}_b)^T \mathbf{B}^{-1}(\mathbf{x}_a - \mathbf{x}_b) + \frac{1}{2}[H(\mathbf{x}_a) - \mathbf{y}]^T \mathbf{R}^{-1}[H(\mathbf{x}_a) - \mathbf{y}], \quad (1)$$

270 where  $\mathbf{x}_a$  is a vector of the analysis field,  $\mathbf{x}_b$  is the background field,  $\mathbf{y}$  is the vector  
 271 of observations,  $\mathbf{B}$  and  $\mathbf{R}$  are the background and observation error covariance matrices,

272 respectively, representing the relative contributions to the analysis, and  $H$  is the  
273 observation operator that maps the model variables to the observation space.

274 The analysis variables were the 3D mass concentrations of the pollution components  
275 (e.g. CO and sulfate) at each grid point. Hourly mean surface pollution observations  
276 within a one-hour window of the analysis were assimilated. To assimilate the surface  
277 pollution observations, model-simulated compositions were first diagnosed at  
278 observation locations. For gas concentrations to be directly used as analysis variables,  
279 the units need to be converted from ppm and ppb to  $\text{mg m}^{-3}$  and  $\mu\text{g m}^{-3}$ , respectively, to  
280 match the observations. The model-simulated  $\text{PM}_{2.5}$  and  $\text{PM}_{10}$  concentrations at the  
281 ground level were diagnosed as follows:

$$282 \quad PM_{2.5} = f_i \times PM_i + f_j \times PM_j + f_k \times PM_k = \text{OC} + \text{EC} + \text{SO}_4^{2-} + \text{NO}_3^- + \text{NH}_4^+ + \\ 283 \quad \text{SEAS} + \text{AP}_{2.5} \quad (2)$$

$$284 \quad PM_{10} = PM_i + PM_j + PM_k = PM_{2.5} + \text{PMC} \quad (3)$$

285 where  $f_i$ ,  $f_j$ , and  $f_k$  are the  $\text{PM}_{2.5}$  fractions of the Aitken, accumulation, and coarse  
286 modes, respectively. These ratios are recommended as the concentrations of  $\text{PM}_{2.5}$  and  
287 fine mode aerosols (i.e. Aitken plus accumulation) can differ because  $\text{PM}_{2.5}$  particles  
288 include small tails from the coarse mode in the CMAQ model (Binkowski and Roselle,  
289 2003; Jiang et al., 2006).  $PM_i$ ,  $PM_j$ , and  $PM_k$  are the mass concentrations of the three  
290 modes in the CMAQ model, respectively. Seven aerosol species of  $\text{PM}_{2.5}$  (organic  
291 carbon (OC), elemental carbon (EC), sulfate ( $\text{SO}_4^{2-}$ ), nitrate ( $\text{NO}_3^-$ ), ammonium ( $\text{NH}_4^+$ ),  
292 sea salt (SEAS), and fine-mode unspiciated aerosols ( $\text{AP}_{2.5}$ )) and additional coarse  
293  $\text{PM}_{10}$  (PMC) were extracted as analysis variables and were updated using the  $\text{PM}_{2.5}$  and  
294 PMC observations. Before calculating equation (1) within the GSI, the analysis  
295 variables were bilinearly interpolated in the horizontal direction to the observation  
296 locations.

297 Calculating background error covariance ( $\mathbf{B}$ ) is generally costly and difficult when a  
298 high-dimensional numerical model is used. For simplification,  $\mathbf{B}$  was represented as a

299 product of spatial correlation matrices and standard deviations (SDs).

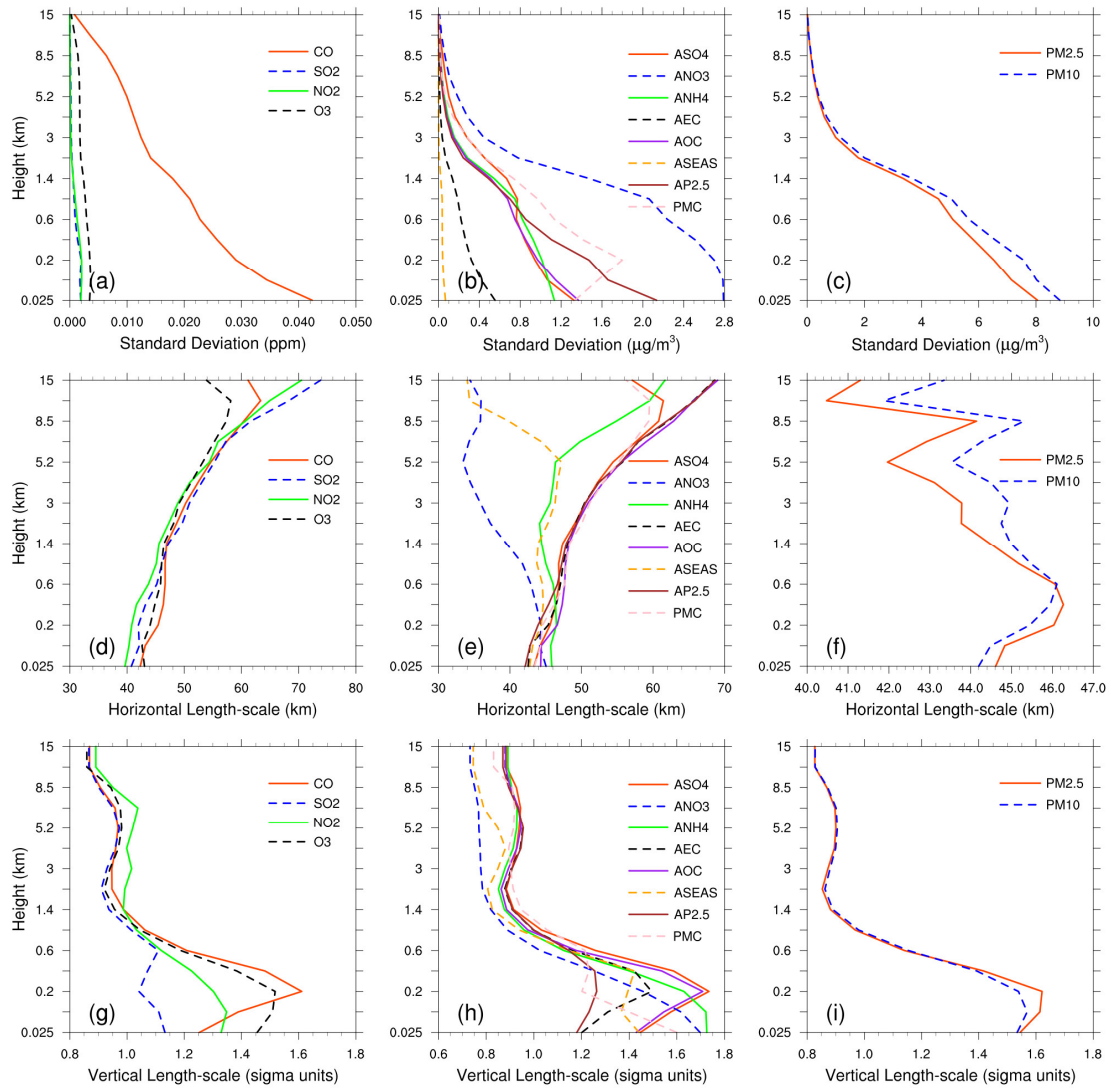
$$300 \quad \mathbf{B} = \mathbf{D}\mathbf{C}\mathbf{D}^T \quad (4)$$

$$301 \quad \mathbf{C} = \mathbf{C}_x \otimes \mathbf{C}_y \otimes \mathbf{C}_z \quad (5)$$

302 where  $\mathbf{D}$  is the background error SD matrix;  $\mathbf{C}$  is the background error correlation  
303 matrix;  $\otimes$  is the Kronecker product; and  $\mathbf{C}_x$ ,  $\mathbf{C}_y$ , and  $\mathbf{C}_z$  denote three one-  
304 dimensional correlation submatrices in the longitude, latitude, and vertical coordinate  
305 directions, respectively.  $\mathbf{C}_x$  and  $\mathbf{C}_y$  are assumed to be horizontally isotropic such that  
306 they can be represented using a Gaussian function. The correlation between any two  
307 points  $x_i$  and  $x_j$  in the horizontal direction is expressed as follows:

$$308 \quad c(x_i, x_j) = e^{-\frac{(x_i-x_j)^2}{2L^2}} \quad (6)$$

309 where  $L$  is the horizontal correlation scale estimated using the proxy of the  
310 background error (Figure 3). The vertical correlation matrix  $\mathbf{C}_z$  is directly estimated  
311 from the model background field as  $\mathbf{C}_z$  is only an  $n_z \times n_z$  (here,  $n_z=15$ ) matrix.



312

313 **Figure 3.** Vertical profiles of standard deviations (top,  $\mu\text{g m}^{-3}$ ), horizontal (middle, km)  
 314 and vertical (bottom, km) length scales for CO, SO<sub>2</sub>, NO<sub>2</sub>, O<sub>3</sub>, sulfate, nitrate,  
 315 ammonium, EC, OC, sea salt, unsciated aerosols (AP<sub>2.5</sub>), PMC, PM<sub>2.5</sub> and PM<sub>10</sub>.

316 To estimate these matrices, the “NMC” method was used to compute **B** for each variable  
 317 by taking the differences between forecasts of different lengths valid at the same time  
 318 (Parrish and Derber, 1992; Rabier et al., 1998). Differences between the 24- and 12-h  
 319 WRF/CMAQ forecasts of 60 pairs (two pairs per day) of analysis variables valid at  
 320 either 0000 or 1200 UTC over November 2016 were used. The horizontal and vertical  
 321 length scales of the correlation matrices were estimated using recursive filters (Purser  
 322 et al., 2003). The vertical distribution of the background error SDs, which varies with  
 323 height and species, is shown in Figure 3. The vertical profile of the background error

324 SDs corresponds to the vertical concentration distribution. This means that higher  
325 concentrations tend to have larger background error SDs (e.g., CO and nitrate). These  
326 SDs exhibit a common reduction as the height increases, especially at the top of the  
327 boundary layer. The horizontal correlation of the background error determines the  
328 propagation of observation information in this direction, whereas the vertical  
329 correlation determines the vertical extension of such increments. For gaseous pollutants  
330 and most individual aerosol components, the horizontal length scales increased with  
331 height, whereas for the total particulate matter (i.e. PM<sub>2.5</sub>, PM<sub>10</sub>), the scales increased  
332 with height in the boundary layer and decreased with height in the free troposphere.  
333 The ground-level scale generally spread 40–45 km for all control variables. The vertical  
334 length scale of most species first increased and then decreased with height, which may  
335 be related to vertical mixing (Kahnert, 2008) and stack emissions at approximately 200  
336 m height.

#### 337 **2.1.4 EnKF assimilation algorithm**

338 In EnKF, the time-dependent uncertainties of the state variables are estimated using a  
339 Monte Carlo approach through an ensemble. Uncertainty can be propagated using linear  
340 or nonlinear dynamic models (flow-dependent background error covariance) by simply  
341 implementing ensemble simulations. The EnSRF algorithm introduced by Bierman  
342 (1977) and Maybeck (1979) was used to constrain pollution emissions in this study.  
343 EnSRF is a deterministic EnKF that obviates the need to perturb observations, which  
344 has a higher computational efficiency and a better performance (Sun et al., 2009).

345 The perturbation of the prior emissions represents the uncertainty. We implemented  
346 additive emission adjustment methods, which were calculated using the following  
347 function:

$$348 \quad \mathbf{X}_i^b = \mathbf{X}_0^b + \delta \mathbf{X}_i^b, i = 1, 2, \dots, N \quad (7)$$

349 where  $\mathbf{b}$  is the background (prior) state,  $i$  is the identifier of the perturbed samples,  
350 and  $N$  is the ensemble size, which was set to 40 considering the trade-off between  
351 computational cost and inversion accuracy (Figure S1). In contrast to the estimation of

throughout?

352 parameters based on the augmentation of the conventional state vector (e.g.  
 353 concentrations) with the parameter variables,  $\mathbf{X}$  only comprises emissions in this study  
 354 (similarly hereafter).  $\delta\mathbf{X}_i^b$  is the randomly perturbed samples added to the prior  
 355 emissions  $\mathbf{X}_0^b$  to produce ensemble samples of the inputs  $\mathbf{X}_i^b$ .  $\delta\mathbf{X}_i^b$  is drawn from  
 356 Gaussian distributions with a mean of zero and standard deviation of the prior emission  
 357 uncertainty in each grid. The state variables of the emissions include CO, SO<sub>2</sub>, NO<sub>x</sub>,  
 358 primary PM<sub>2.5</sub> (PPM<sub>2.5</sub>) and PMC. We used variable localization to update the analysis,  
 359 which means that the covariance among different state variables was not considered,  
 360 and the emission of one species was constrained only by its corresponding air pollutant  
 361 observation. This method has been widely used in chemical data assimilation systems  
 362 to avoid spurious correlations between species (Ma et al., 2019; Miyazaki et al., 2012b).  
 363 After obtaining an ensemble of state vectors (prior emissions), ensemble runs of the  
 364 CMAQ model were conducted to propagate the errors in the model with each ensemble  
 365 sample of state vectors. Combined with the observational vector  $\mathbf{y}$ , the state vector  $\overline{\mathbf{X}}^b$   
 366 was updated by minimizing the analysis variance.

367 
$$\overline{\mathbf{X}}^a = \overline{\mathbf{X}}^b + \mathbf{K}(\mathbf{y} - \mathbf{H}\overline{\mathbf{X}}^b) \quad (8)$$

368 
$$\mathbf{K} = \mathbf{P}^b \mathbf{H}^T (\mathbf{H} \mathbf{P}^b \mathbf{H}^T + \mathbf{R})^{-1} \quad (9)$$

369 
$$\mathbf{P}^b = \frac{1}{N-1} \sum_{i=1}^N (\mathbf{X}_i^b - \overline{\mathbf{X}}^b) (\mathbf{X}_i^b - \overline{\mathbf{X}}^b)^T \quad (10)$$

370 
$$\delta\mathbf{X}_i^a = \delta\mathbf{X}_i^b - \tilde{\mathbf{K}} \mathbf{H} \delta\mathbf{X}_i^b \quad (11)$$

371 While employing sequential assimilation and independent observations,  $\tilde{\mathbf{K}}$  is  
 372 calculated as follows:

373 
$$\tilde{\mathbf{K}} = \left( 1 + \sqrt{\mathbf{R} / (\mathbf{H} \mathbf{P}^b \mathbf{H}^T + \mathbf{R})} \right)^{-1} \mathbf{K} \quad (12)$$

374 where  $\overline{\mathbf{X}}^b$  is the mean of the ensemble samples  $\mathbf{X}_i^b$ ;  $\mathbf{H}$  is the observation operator that  
 375 maps the model space to the observation space, consisting of the model integration

Fluxes



unclear, please rephrase  
H<sup>T</sup>: Concentration →

376 process converting emissions into concentrations and spatial interpolation matching the  
 377 model concentration to the locations of the observations;  $\mathbf{y} - \mathbf{H}\bar{\mathbf{X}}^b$  reflects the  
 378 differences between the simulated and observed concentrations;  $\mathbf{P}^b$  is the ensemble-  
 379 estimated background (a priori) error covariance;  $\mathbf{P}^b \mathbf{H}^T$  contains the response of the  
 380 uncertainty in the simulated concentrations to the uncertainty in emissions;  $\mathbf{K}$  is the  
 381 Kalman gain matrix of the ensemble mean depending on the  $\mathbf{P}^b$  and observation error  
 382 covariance  $\mathbf{R}$ , representing the relative contributions to analysis; and  $\tilde{\mathbf{K}}$  is the Kalman  
 383 gain matrix of the ensemble perturbation, which is used to calculate emission  
 384 perturbations after inversions  $\delta \mathbf{X}_i^a$ . The ensemble mean  $\bar{\mathbf{X}}^a$  of the analyzed state was  
 385 considered the best estimate of the emissions.

386 When large volumes of site observations are at a much higher resolution than the model  
 387 grid spacing, many correlated or fully consistent model-data mismatch errors can  
 388 appear in one cluster, resulting in excessive adjustments and deteriorated model  
 389 performance (Houtekamer and Mitchell, 2001). To reduce the horizontal observation  
 390 error correlations and influence of representativeness errors, a “super-observation”  
 391 approach combining multiple noisy observations located within the same grid and  
 392 assimilation window was developed based on optimal estimation theory (Miyazaki et  
 393 al., 2012a). Previous studies demonstrated the necessity for data-thinning and  
 394 dealiasing errors (Feng et al., 2020b; Zhang et al., 2009a). The super-observation  $y_{new}$ ,  
 395 super-observation error  $r_{new}$ , and corresponding simulation  $x_{new,i}$  of the  $i$ th sample  
 396 are calculated as follows:

397 
$$1/r_{new}^2 = \sum_{j=1}^m 1/r_j^2 \quad (13)$$

398 
$$y_{new} = \sum_{j=1}^m w_j y_j / \sum_{j=1}^m w_j \quad (14)$$

399 
$$x_{new,i} = \sum_{j=1}^m w_j x_{ij} / \sum_{j=1}^m w_j \quad (15)$$

400 where  $j$  is the identifier of  $m$  observations within a super-observation grid;  $r_j$  is the  
 401 observational error of the actual  $j$ th observation  $y_j$ ;  $x_{ij}$  is the simulated concentration

per grid cell?

402 using the  $i$ th prior emission sample corresponding to the  $j$ th observation; and  $w_j =$   
403  $1/r_j^2$  is the weighting factor. The super-observation error decreased as the number of  
404 observations used within a super-observation increased. This method was used in our  
405 previous inversions using surface-based (Feng et al., 2020b) and satellite-based (Jiang  
406 et al., 2021) observations.

407 In this study, the DA window was set to one day because the model requires a longer  
408 time to integrate the emission information into the ~~concentration~~ ensembles (Ma et al.,  
409 2019). Due to the “super-observation” approach, only one assimilation is needed in one  
410 assimilation window. In addition, owing to the complexity of hourly emissions, it is  
411 difficult to simulate hourly concentrations that match the observations well. Although  
412 a longer DA window would allow more observations to constrain the emission change  
413 of one grid, the spurious correlation signals of EnKF would attenuate the observation  
414 information over time (Bruhwiler et al., 2005; Jiang et al., 2021). Kang et al. (2012)  
415 conducted OSSEs and demonstrated that owing to the transport errors and increased  
416 spurious correlation, a longer DA window (e.g. 3 weeks) would cause the analysis  
417 system to blur essential emission information away from the observation. Therefore,  
418 daily mean simulations and observations were used in the EnSRF algorithm and daily  
419 emissions were optimized in this system.

420 EnKF is subject to spurious correlations because of the limited number of ensembles  
421 when it is applied in high-dimensional atmospheric models, which can cause rank  
422 deficiencies in the estimated background error covariance and filter divergence and  
423 further degrade analyses and forecasts (Wang et al., 2020). Covariance localization is  
424 performed to reduce spurious correlations caused by a finite ensemble size  
425 (Houtekamer and Mitchell, 2001). Covariance localization preserves the meaningful  
426 impact of observations on state variables within a certain distance (cutoff radius) but  
427 limits the detrimental impact of observations on remote state variables. The localization  
428 function of Gaspari and Cohn ~~function~~ (Gaspari and Cohn, 1999) is used in this system,

o

429 which is a piecewise continuous fifth-order polynomial approximation of a normal  
430 distribution. The optimal localization scale is related to the ensemble size, assimilation  
431 window, dynamic system, and lifetime of the chemical species in the atmosphere. CO,  
432 SO<sub>2</sub> and PM<sub>2.5</sub> are rather stable in the atmosphere, with a lifetime of more than one day.  
433 According to the average wind speed (3.3 m/s, Table 4) and length of the DA window,  
434 the localization scales of CO, SO<sub>2</sub> and PM<sub>2.5</sub> were set to 300 km. In addition, the  
435 localization scales of NO<sub>2</sub>, which is rather reactive and has a lifetime of approximately  
436 10 hours in winter (de Foy et al., 2015), and PMC, which ~~is~~ mainly from local sources  
437 and has a short residence time in the atmosphere owing to the rapid deposition rate  
438 (Clements et al., 2014; Clements et al., 2016; Hinds, 1982), were set to 150 and 250  
439 km, respectively.

Verb  
missing

## 440 2.2 Prior emissions and uncertainties

441 Anthropogenic emissions over China were obtained from the 2016 Multi-resolution  
442 Emission Inventory for China (MEIC 2016) (Zheng et al., 2018), while those over the  
443 other regions of East Asia were obtained from the mosaic Asian anthropogenic emission  
444 inventory (MIX) (Li et al., 2017). The spatial resolutions of the MEIC and MIX  
445 inventories were both 0.25° × 0.25° and they are downscaled to match the model grid  
446 spacing of 36 km. The spatial distributions of CO, SO<sub>2</sub>, NO<sub>x</sub>, PPM<sub>2.5</sub>, and PMC  
447 emissions are shown in Figure 11. The daily emission inventory, which was  
448 arithmetically averaged from the combined monthly emission inventory, was directly  
449 used in the EI subsystem and was employed as the prior emission of the first DA  
450 window in the EI subsystem (Figure 1). During the simulations, daily emissions were  
451 further converted to hourly emissions. All species emitted from area sources were  
452 converted to hourly emissions using the same diurnal profile (Figure S2) and for the  
453 point source, we assumed that there was no diurnal change. MEIC 2012 was used as an  
454 alternative a priori over China to investigate the impact of different prior emissions on  
455 optimized emissions. The Model of Emissions of Gases and Aerosols from Nature  
456 (MEGAN) (Guenther et al., 2012) was used to calculate time-dependent biogenic  
457 emissions, which was driven by the WRF model. Biomass burning emissions were not

458 included because they have little impact across China during the study period (Zhang  
459 et al., 2020).

460 During the inversion cycles, inverted emissions of different members converge  
461 gradually, and the ensemble-estimated error covariance matrix is likely to be  
462 underestimated. To avoid this, considering the compensation of model errors and  
463 comparable emission uncertainties from one day to the next, we imposed the same  
464 uncertainty on emissions at each DA window. As mentioned above, the optimized  
465 emissions of the current DA window were transferred to the next DA window as prior  
466 emissions. The technology-based emission inventory developed by Zhang et al. (2009b),  
467 using the same method as MEIC, showed that the emissions of PMC and PPM<sub>2.5</sub> had  
468 the largest uncertainties, followed by CO, and finally SO<sub>2</sub> and NO<sub>x</sub>. Therefore, the  
469 uncertainties of PMC, PPM<sub>2.5</sub>, CO, SO<sub>2</sub>, and NO<sub>x</sub> in this study were set as 40%, 40%,  
470 30%, 25%, and 25%, respectively. However, previous studies have shown that inversely  
471 estimated CO and PMC emissions can exceed 100% higher than the bottom-up  
472 emissions (MEIC) in certain areas (Feng et al., 2020b; Ma et al., 2019). Therefore,  
473 according to the extent of underestimation, we set an uncertainty of 100% for both the  
474 CO and PMC emissions at the beginning of the three DA windows to quickly converge  
475 the emissions. Mean emission analysis is generally minimally sensitive to the  
476 uncertainty setting in the assimilation cycle method (Feng et al., 2020; Gurney et al.,  
477 2004; Miyazaki et al., 2012a) as the inversion errors of the current window can be  
478 transferred to the next window for further optimization (Section 4.3).

### 479 **2.3 Observation data and errors**

480 Hourly averaged surface CO, SO<sub>2</sub>, NO<sub>2</sub>, O<sub>3</sub>, PM<sub>2.5</sub>, and PM<sub>10</sub> observations from 1504  
481 national control air quality stations were assimilated into this system, which were  
482 obtained from the Ministry of Ecology and Environment of the People's Republic of  
483 China (<http://106.37.208.233:20035/>, last access: 25 June 2020). These sites are  
484 distributed over most of central and eastern China and become denser near metropolitan  
485 areas (see Figure 2). To ensure data quality, value-range checks were performed to  
486 eliminate unrealistic or unrepresentative observations and only the observations within

487 the subjectively selected threshold range were assimilated (Table 2). In additionally, a  
488 time-continuity check was performed to eliminate gross outliers and sudden anomalies  
489 using the function of  $\max(|O(t) - O(t \pm 1)|) \leq f(t)$ , where  $O(t)$  and  $O(t \pm 1)$   
490 represent observations at time  $t$  and  $t \pm 1$ , respectively, and  $f(t) = T_a + T_b \times O_t$ .  
491 This means that the concentration difference between time  $t$  and time  $t+1$  and  $t-1$  should  
492 be less than  $f(t)$ .  $T_b$  was fixed at 0.15 and the section of  $T_a$  is given in Table 2,  
493 which was determined empirically according to the time series change of concentration  
494 at each site. To avoid potential cross-correlations, we assimilated PM<sub>2.5</sub> and PMC.  
495 Additionally, in the EI subsystem, the observations within each city were averaged to  
496 reduce the data density, reduce the error correlation, and increase spatial representation  
497 (Houtekamer and Mitchell, 2001; Houtekamer and Zhang, 2016). Finally, 336 city sites  
498 were available across mainland China, in which data from 311 cities were selected for  
499 assimilation and the remaining 25 were selected for independent validation (Figure 2).  
500 In the IA subsystem, owing to the small horizontal correlation scale (Figure 3), all site  
501 observations were assimilated to provide a good IC for the next emission inversion to  
502 obtain more extensive observation constraints.

503 The observation error covariance matrix ( $\mathbf{R}$ ) includes both the measurement and  
504 representation errors. The measurement error  $\varepsilon_0$  is defined as follows:

$$505 \quad \varepsilon_0 = ermax + ermin \times \Pi_0 \quad (16)$$

506 where  $ermax$  is the base error and  $\Pi_0$  denotes the observed concentration. These  
507 parameters for different species are listed in Table 2 and were determined according to  
508 Chen et al. (2019), Feng et al. (2018), and Jiang et al. (2013b).

509 The representative error depends on the model resolution and characteristics of the  
510 observation locations, which were calculated using the equations of Elbern et al. (2007),  
511 defined as follows:

$$512 \quad \varepsilon_r = \gamma \varepsilon_0 \sqrt{\Delta l / L} \quad (17)$$

513 where  $\gamma$  is a tunable parameter (here,  $\gamma=0.5$ ),  $\Delta l$  is the grid spacing (36 km), and  $L$

514 is the radius (3 km for simplification) of the influence area of the observation. The total  
 515 observation error ( $r$ ) was defined as follows:

$$516 \quad r = \sqrt{\varepsilon_0^2 + \varepsilon_r^2} \quad (18)$$

517 **Table 2.** Parameters of quality control and measurement error

Parameter	CO mg m <sup>-3</sup>	SO <sub>2</sub> μg m <sup>-3</sup>	NO <sub>2</sub> μg m <sup>-3</sup>	O <sub>3</sub> μg m <sup>-3</sup>	PM <sub>2.5</sub> μg m <sup>-3</sup>	PMC μg m <sup>-3</sup>
value-range	0.1-12	1-800	1-250	1-250	1-800	1-900
time-continuity ( $T_a$ )	2.5	160	70	80	180	180
ermax	0.05	1	1	1	1.5	1.5
ermin	0.5%	0.5%	0.5%	0.5%	0.75%	0.75%

518

### 519 **3 Experimental design**

*simulations were?  
or "RAPAS was used..."*

520 RAPAS was conducted according to the procedure and settings described in Section 2.  
 521 December is one of the months with the most severe air pollution, whereas July is one  
 522 of the least polluted months in China. Therefore, this study mainly tested the  
 523 performance of the RAPAS system over these two months. For December, the IA  
 524 subsystem was run from 26 November to 31, 2016, with a 6-hour interval cycling  
 525 assimilation to optimize ICs (ICDA). A better IC at 0000 UTC on 1 December could be  
 526 obtained by a five-day high-frequency cycling assimilation and atmospheric mixing.  
 527 The EI subsystem was then run for December 2016 with a one-day assimilation window  
 528 to optimize emissions (EMDA). In July, the system operated identically to that of  
 529 December. It should be noted that owing to the stronger atmospheric oxidation, the  
 530 lifetime of NO<sub>2</sub> in July was significantly shorter than that in December; thus, we  
 531 adopted a smaller localization scale for NO<sub>2</sub> (80 km). Both assimilation experiments  
 532 used the combined prior emission inventories of 2016, as described in Section 2.2, and  
 533 the emission base year coincided with the research stage. An Observing Systems  
 534 Simulation Experiment (OSSE) was conducted to evaluate the performance of the

"performed" or "run"

535 RAPAS system, which has been widely used in previous assimilation systems  
536 development (Daley, 1997). In the OSSE experiment, we used the MEIC 2016  
537 inventory as a "true" emission and reduced by 30% over mainland China as a prior  
538 emission. The simulations were ~~simulated~~ using the "true" emission and sampled  
539 according to the locations and times of the real observations used as artificial  
540 observations. The observation errors were the same as those in EMDA. To evaluate the  
541 IC improvements from the IA subsystem, an experiment without 3DVAR (NODA) was  
542 conducted with the same meteorological fields and physical and chemistry  
543 parameterization settings as those of the ICDA. To evaluate the posterior emissions of  
544 the EI subsystem, two parallel forward modelling experiments were performed for  
545 December 2016: a control experiment (CEP) with prior (MEIC 2016) emissions and a  
546 validation experiment (VEP) with posterior emissions. Both experiments used the same  
547 IC at 0000 UTC on December 01 generated through the IA subsystem. The only  
548 difference between CEP and VEP were emissions. Table 3 summarizes the different  
549 emission inversion experiments conducted in this study.

Seven?

550 To investigate the robustness of our system, eight sensitivity tests (from EMS1 to EMS7;  
551 see Table 3) were performed. These experiments were all based on EMDA. EMS1 used  
552 MEIC 2012 as the original prior emission in China, aiming to investigate the impact of  
553 different prior inventories on the estimates of emissions. The other experiments  
554 (EMS2–5) aimed to test the impact of different prior uncertainty settings, in which the  
555 prior uncertainties were reduced by -50% and -25%, and increased by 25% and 50%,  
556 respectively. EMS6 aimed to evaluate the impact of observation errors on emission  
557 estimates, in which all observation errors are magnified twice. EMS7 aimed to evaluate  
558 the impact of IC optimization of the first window on emission estimates, in which the  
559 ICs were taken from a five-day spin-up simulation. Eight forward modelling  
560 experiments (VEP1, VEP2, ..., VEP7) were also performed with the posterior  
561 emissions of EMS1 to EMS7 to evaluate their performance.

562

563 **Table 3.** Emission inversion and sensitivity experiments conducted in this study

Exp. Type	Exp. Name	Period	IC of the first DA Window	ICs of the subsequent DA window	Emission
Assimilation	EMDA	1–31 December	0000 UTC on December 1, taken from ICDA	Forecast with posterior emissions in the previous window	MEIC 2016 for December (the first DA window), optimized emissions of the previous window (other DA windows)
	OSSE	1–31 December	Same as EMDA	Same as EMDA	Same as EMDA but with a decrease of 30% for CO, SO <sub>2</sub> , NO <sub>x</sub> , PPM <sub>2.5</sub> , and PMC
Sensitivity	EMS1	1–31 December	Same as EMDA	Same as EMDA	Same as EMDA but for EMIC 2012
	EMS2-5	1–31 December	Same as EMDA	Same as EMDA	Same as EMDA but with a ± 25% or ± 50% of default uncertainty
	EMS6	1–31 December	Same as EMDA	Same as EMDA	Same as EMDA but with a +100% of default observation errors
	EMS7	1–31 December	0000 UTC on December 1, taken from ICNO	Same as EMDA	Same as EMDA

564

565 **4 Results**566 **4.1 Evaluations**567 **4.1.1 Simulated meteorological fields**

568 In the RAPAS system, the inversion approach attributes all biases between the  
569 simulated and observed concentrations to emissions. Meteorological fields dominate  
570 the physical and chemical processes of air pollutants in the atmosphere, and thus their



571 simulation accuracy would significantly affect the estimates of emissions in this study.  
572 To quantitatively evaluate the performance of the WRF simulations, the mean bias  
573 (BIAS), root mean square error (RMSE), and correlation coefficient (CORR) were  
574 calculated against the surface meteorological observations measured at 400 stations and  
575 the planetary boundary layer height (PBLH) was calculated using the sounding data at  
576 92 sites. Surface observations were obtained from the National Climate Data Center  
577 integrated surface database (<http://www.ncdc.noaa.gov/oa/ncdc.html>, last access: 25  
578 October 2021) and sounding data were obtained from the website of the University of  
579 Wyoming (<http://weather.uwyo.edu/upperair/sounding.html>, last access: 10 March  
580 2022). The sounding data had a 12 hour interval. The observed PBLH was calculated  
581 using sound data via the bulk Richardson number method (Richardson et al., 2013).  
582 The spatial distribution of meteorological stations is shown in Figure 2. The simulated  
583 temperature at 2 m (T2), relative humidity at 2 m (RH2), wind speed at 10 m (WS10),  
584 and PBLH from 26 November to 31 December 2016 were evaluated against the  
585 observations. Table 4 summarizes the statistical results of the evaluation of the  
586 simulated meteorological parameters. Overall, T2, RH2 and PBLH were slightly  
587 underestimated, with biases of -0.1 °C, -3.8%, and -41.1 m, respectively. CORRs were  
588 approximately 0.98 for T2, 0.94 for RH2, and 0.90 for PBLH, showing good  
589 consistency between the observations and simulations. WS10 was overestimated, with  
590 a bias of 0.7 m/s and an RMSE of 0.8 m/s, but were better than the simulations from  
591 many previous studies (Chen et al., 2016; Jiang et al., 2012a; Jiang et al., 2012b).  
592 Therefore, the WRF can generally reproduce meteorological conditions sufficiently in  
593 terms of their temporal variation and magnitude over China, which is adequate for our  
594 inversion estimation.

595

596

597

598

599 **Table 4.** Statistics comparing the simulated and observed 10-m wind speed (WS10), 2-  
600 m temperature (T2), and 2-m relative humidity (RH2), and planetary boundary layer  
601 height (PBLH).

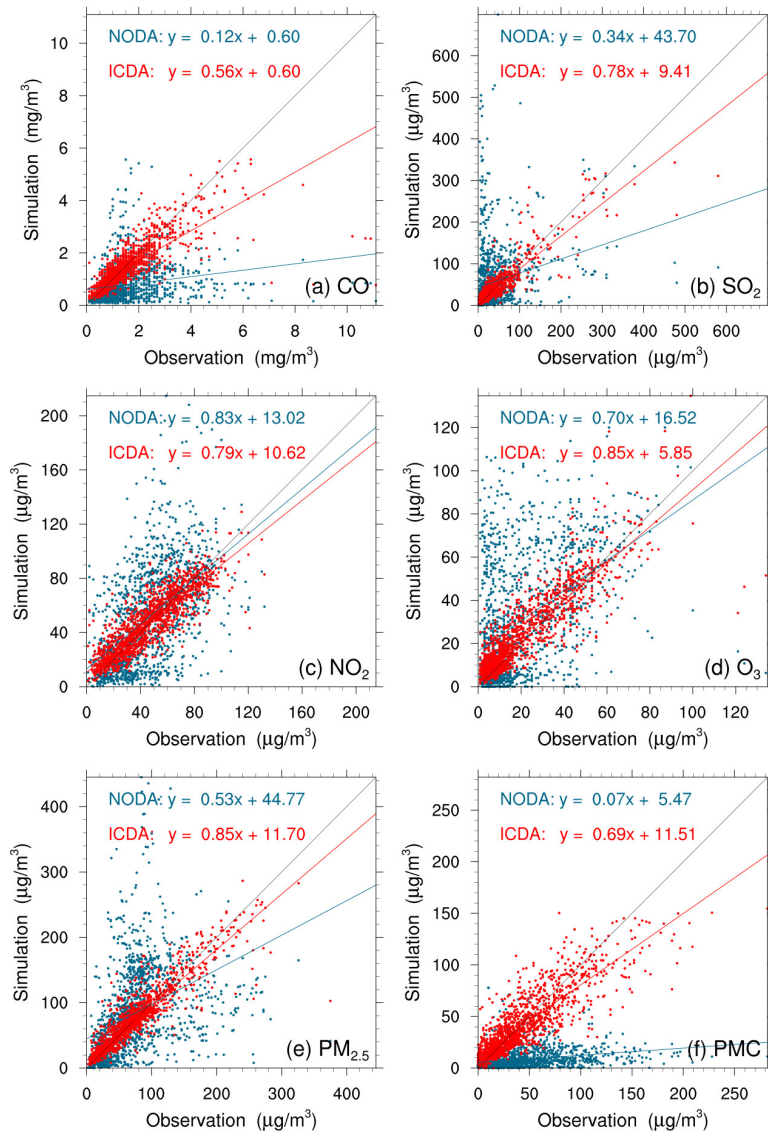
Variable Met.	No. of sites	Mean Obs.	Mean Sim.	BIAS	RMSE	CORR
WS10 (m/s)	400	2.6	3.3	0.7	0.8	0.72
T2 (°C)	400	2.9	2.8	-0.1	0.7	0.98
RH2 (%)	400	66.3	62.6	-3.8	5.2	0.94
PBLH (m)	92	267.5	226.4	-41.1	50.4	0.90

602 \* BIAS, mean bias; RMSE, root mean square error; CORR, correlation coefficient

#### 603 4.1.2 Initial conditions

604 Figure 4 shows an evaluation of the analyzed concentrations of the six species against  
605 surface observations. For comparison, the evaluations of the simulations without  
606 3DVAR (NODA) are also shown in Figure 4. The simulations of the NODA experiment  
607 (red dots) are scattered on both sides of the central line, as large systematic biases  
608 remain across many measurement sites. Conversely, the ICDA experiment (blue dots)  
609 showed a much better agreement with the observations than those from NODA. The  
610 statistics show that there are large systematic biases in the NODA simulations, with  
611 large RMSEs and small CORRs for all species, particularly for CO and PMC. After the  
612 assimilation of surface observations, the RMSE of CO decreased to 0.7 mg m<sup>-3</sup>, and  
613 those of SO<sub>2</sub>, NO<sub>2</sub>, O<sub>3</sub>, PM<sub>2.5</sub>, and PMC decrease to 22.0, 12.0, 9.6, 20.5, and 19.6 μg  
614 m<sup>-3</sup>, respectively, with respective reductions of 50.0%, 73.1%, 61.0%, 64.7%, 69.5%,  
615 and 60.8% compared to those of the NODA (Table 5). The CORRs of ICDA increased  
616 by 290.0%, 291.3%, 55.4%, 87.2%, 130.0%, and 214.8% to 0.78, 0.90, 0.87, 0.88, 0.92,  
617 and 0.85, respectively. These statistics indicate that the ICs of the ground level  
618 improved significantly. However, owing to the lack of observations, we still do not  
619 know the simulation bias in the upper-middle boundary layer. Although concentrations  
620 at high altitudes can be constrained by ground-based observations through vertical

621 correlations, the effect is limited; therefore, the bias remains non-negligible.



622

623 **Figure 4.** Scatter plots of simulated versus observed (a) CO, (b) SO<sub>2</sub>, (c) NO<sub>2</sub>, (d) O<sub>3</sub>,  
624 (e) PM<sub>2.5</sub>, and (f) PMC mass concentrations at 0000 UTC on December 1 initializations  
625 from the background (red) and analysis (blue) fields.

626

627

628

629

630

631 **Table 5.** Comparisons of the surface CO, SO<sub>2</sub>, NO<sub>2</sub>, O<sub>3</sub>, PM<sub>2.5</sub>, and PMC mass  
 632 concentrations from the control and assimilation experiment against observations  
 633 aggregated over all analysis times. CO unit: mg m<sup>-3</sup>; others units: µg m<sup>-3</sup>.

Species	Exp. Name	Mean Obs.	Mean Sim.	BIAS	RMSE	CORR
CO	NODA	1.5	0.8	-0.7	1.4	0.20
	ICDA		1.5	-0.1	0.7	0.78
SO <sub>2</sub>	NODA	36.3	56.0	19.7	81.7	0.23
	ICDA		37.8	1.5	22.0	0.90
NO <sub>2</sub>	NODA	45.8	51.1	5.3	30.8	0.56
	ICDA		47.0	1.1	12.0	0.87
O <sub>3</sub>	NODA	20.5	30.8	10.4	27.2	0.47
	ICDA		23.3	2.8	9.6	0.88
PM <sub>2.5</sub>	NODA	70.9	82.2	11.3	67.3	0.40
	ICDA		71.8	0.9	20.5	0.92
PMC	NODA	43.5	8.5	-35.0	50.0	0.27
	ICDA		41.6	-1.9	19.6	0.85

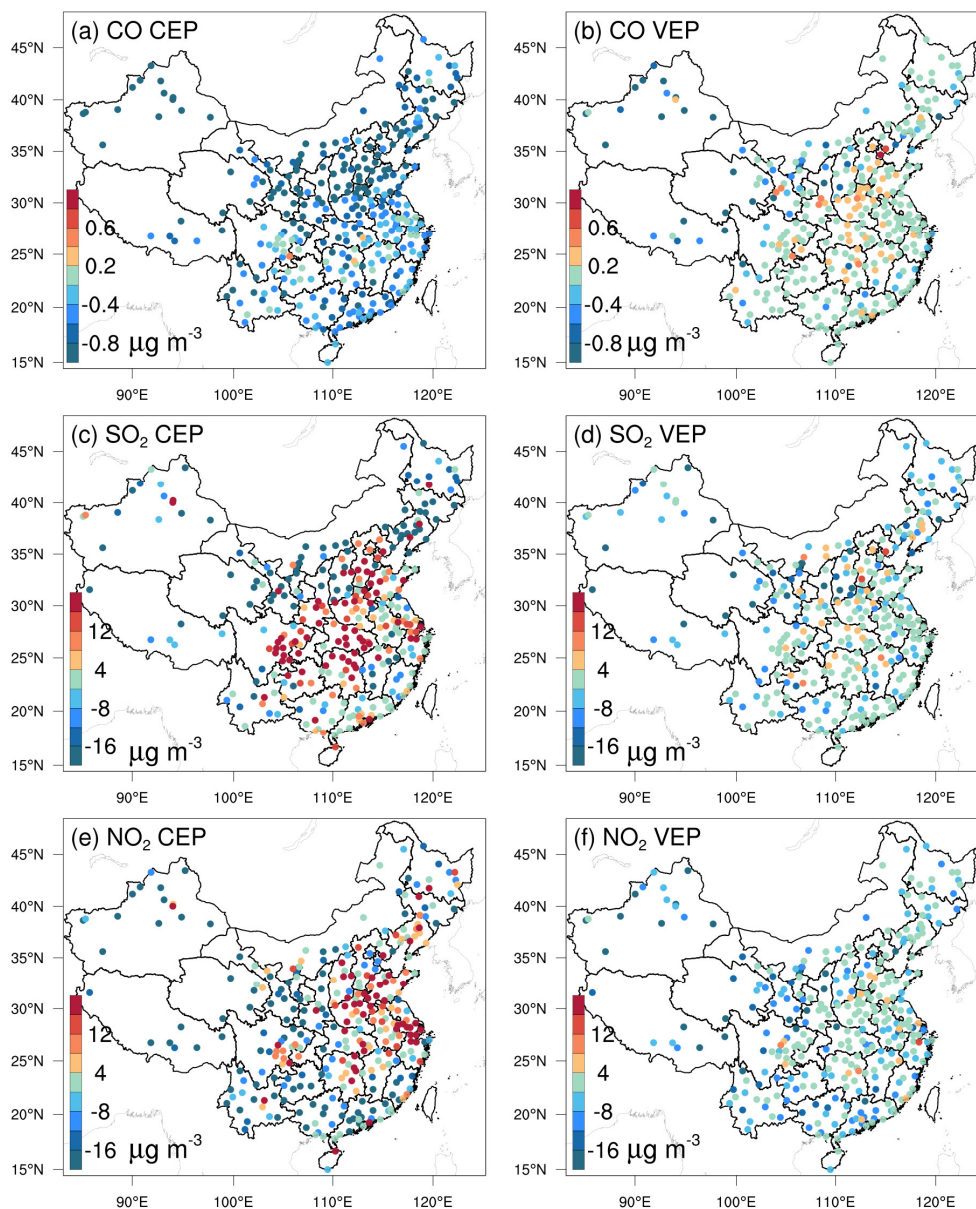
634 \* BIAS, mean bias; RMSE, root mean square error; CORR, correlation coefficient

### 635 4.1.3 Posterior emissions

636 Owing to the mismatched spatial scales, it is difficult to directly evaluate the optimized  
 637 emissions against observations. Generally, we indirectly validated the optimized  
 638 emissions by comparing the forward simulated concentrations using the posterior  
 639 emissions against atmospheric measurements (e.g., Jiang et al., 2014; Jin et al., 2018;  
 640 Peters et al., 2007). Figure 5 shows the spatial distributions of the mean biases between  
 641 the gaseous pollutants simulated using prior and posterior emissions and assimilated  
 642 observations. In the CEPs, for each species, the distribution of biases was similar to the  
 643 increments in background fields constrained through 3DVAR, as shown in Figure S3.  
 644 For example, almost all sites had large negative biases for CO, while for SO<sub>2</sub> and NO<sub>2</sub>,  
 645 positive biases were mainly distributed over the North China Plain (NCP), Yangtze  
 646 River Delta (YRD), Sichuan Basin (SCB), and Central China and negative biases were  
 647 distributed over remaining areas. After constraining with observations, the biases of all

648 three gaseous air pollutants were significantly reduced at most sites. For CO, the biases  
649 at 62% of the sites decreased to absolute values less than  $0.2 \text{ mg m}^{-3}$  and for SO<sub>2</sub> and  
650 NO<sub>2</sub>, the biases at 52% and 47% of the sites were within  $\pm 4 \text{ } \mu\text{g m}^{-3}$ . However, large  
651 negative biases were still observed in western China, indicating that the uncertainties  
652 of the posterior emissions are still large in western China, which may be attributed to  
653 the large biases in prior emissions and the relatively limited observations. Overall, the  
654 statistics show that there are different levels of improvement at the 311 assimilation  
655 sites of 92%, 85%, and 85% for CO, SO<sub>2</sub>, and NO<sub>2</sub>, respectively. The small number of  
656 sites with worse performance may be related to over-adjusted emissions by EI or  
657 contradictory adjustments caused by opposite biases in adjacent areas.

658 Table 6 lists the statistical results of the evaluations averaged over the whole mainland  
659 of China. For CO, the mean bias was  $-0.8 \text{ mg m}^{-3}$  with the prior emissions, while it  
660 substantially reduced to  $-0.1 \text{ mg m}^{-3}$  (reduction rate of 89.6%) when simulating with  
661 the posterior emissions. Additionally, the RMSE decreased by 48.1% from 1.08 to 0.56  
662  $\text{mg m}^{-3}$ , and the CORR increased by 76.1% from 0.46 to 0.81. For SO<sub>2</sub> and NO<sub>2</sub>, the  
663 regional mean biases slightly increased as the positive/negative biases among different  
664 sites might be offset. However, the RMSEs decreased to 17.7 and 12.3  $\mu\text{g m}^{-3}$ ,  
665 respectively, which were 58.3% and 50.8% lower than those of CEPs, and the CORRs  
666 increased by 125.6% and 35.4%, both reaching up to 0.88, indicating that EI  
667 significantly improved the NO<sub>x</sub> and SO<sub>2</sub> emission estimates.

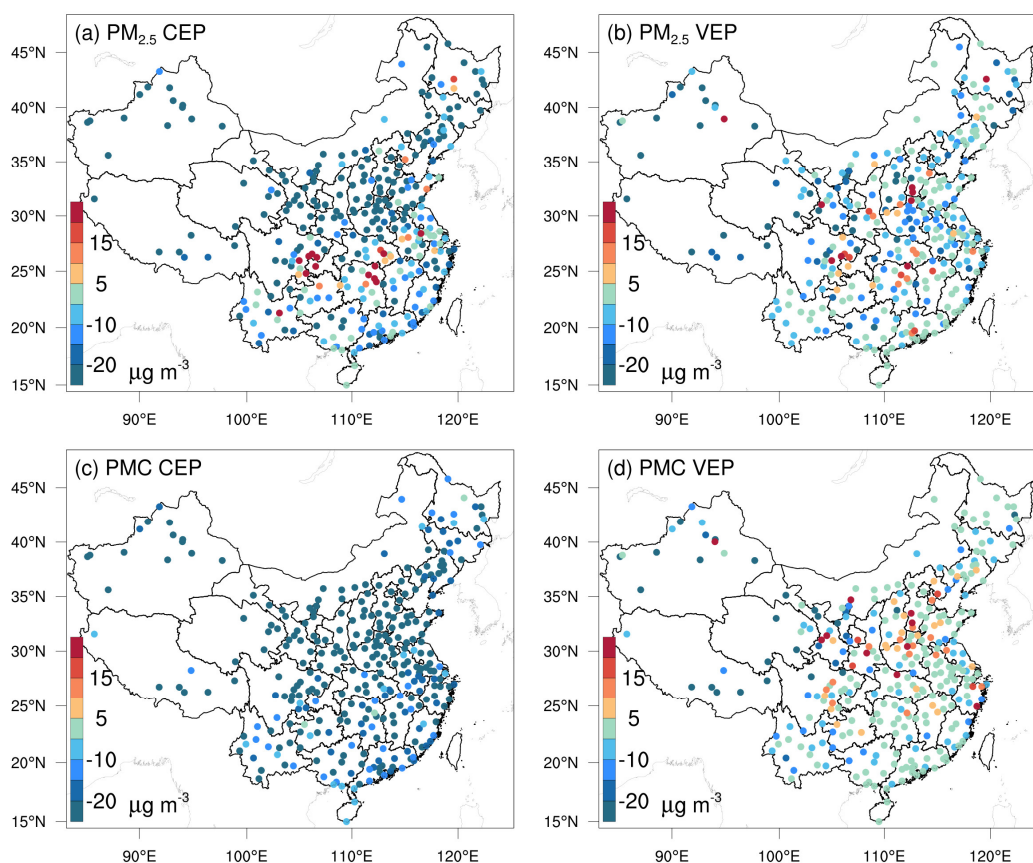


668

669 **Figure 5.** Spatial distribution of the BIAS of the simulated (a, b) CO, (c, d) SO<sub>2</sub>, and  
 670 (e, f) NO<sub>2</sub> with prior (left, CEP) and posterior (right, VEP) emissions. CO unit: mg m<sup>-3</sup>  
 671 <sup>3</sup>; SO<sub>2</sub> and NO<sub>2</sub> units: µg m<sup>-3</sup>.

672 Figure 6 shows the spatial distributions of the mean biases of simulated PM<sub>2.5</sub> and PMC  
 673 evaluated against assimilated observations. Similarly, the CEP simulations did not  
 674 perform well. There were widespread underestimations across the country, with mean  
 675 biases of -24.0 and -32.4 µg m<sup>-3</sup>. After data assimilation, the performance of the VEP  
 676 simulations significantly improved. The biases decreased by 72.1% and 90.4% to -6.7

677 and  $-3.1 \mu\text{g m}^{-3}$ , the RMSEs decreased by 41.2% and 40.7% to 29.6 and  $24.6 \mu\text{g m}^{-3}$ ,  
678 and the CORRs increased by 35.9% and 176.0% to 0.87 and 0.69 for  $\text{PM}_{2.5}$  and PMC,  
679 respectively. Overall, 89.6% and 97.2% of the assimilation sites were improved for  
680  $\text{PM}_{2.5}$  and PMC, respectively. However, compared with the results for the three gaseous  
681 pollutants, there were sites with large biases scattered throughout the entire domain. In  
682 addition to the potential over-adjusted or contradictory adjustments of emissions as in  
683 the three gas species, the sites with large biases may be related to the complex  
684 precursors and complex homogeneous and heterogeneous chemical reactions and  
685 transformation processes of secondary  $\text{PM}_{2.5}$ , and the fact that we did not simulate the  
686 time variation of dust blowing caused by wind speed for PMC owing to the lack of land  
687 cover data that is compatible with the CMAQ dust module and agricultural activity data  
688 to identify dust source regions.

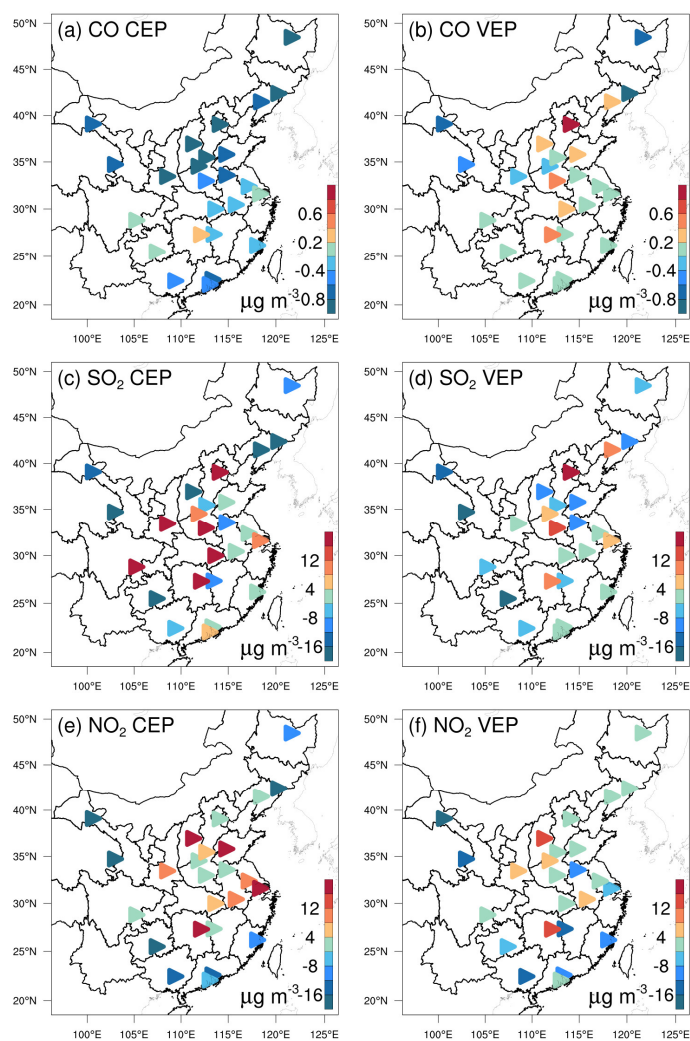


689

690

**Figure 6.** Same as in Figure 5 but for  $\text{PM}_{2.5}$  and PMC.

691 Figures 7 and 8 show the spatial distributions of the biases calculated against  
 692 independent observations for the five species. With posterior emissions, the decreasing  
 693 ratios of RMSEs ranged from 26.7%–42.0% and the CORRs increased by 13.7–59.0%  
 694 to 0.62–0.87. Overall, the biases at the independent sites are similar or slightly worse  
 695 than those at the assimilated sites, which is reasonable as the closer the independent  
 696 sites are to the assimilated site, the more constraints of observation information can be  
 697 obtained and the more significant the improvements in the optimized state variables of  
 698 the model. For example, generally, the transmission distance of NO<sub>2</sub> is relatively short  
 699 and remote cities with small emission correlations to the cities with assimilated  
 700 observations are relatively less constrained, resulting in only a 26.7% decrease in the  
 701 RMSE.

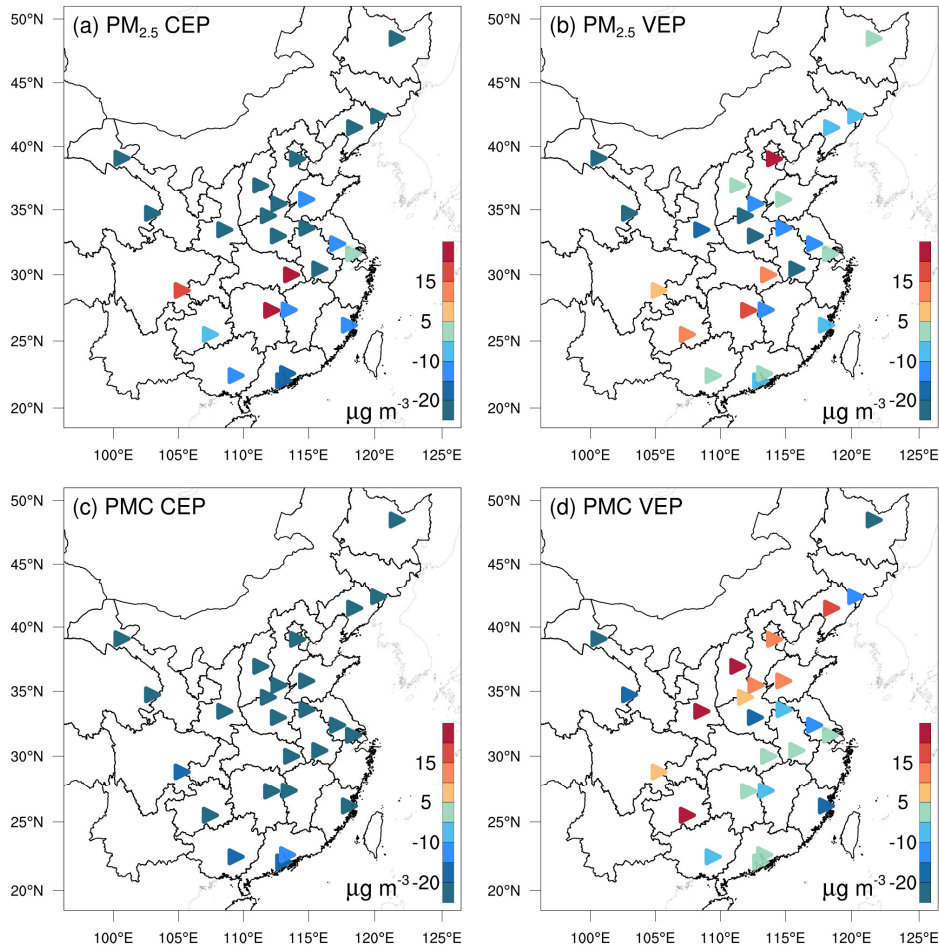


702

703

**Figure 7.** As in Figure 5 but for the independent validation.





704  
705

**Figure 8.** As in Figure 6 but for the independent validation.

706 Comparing our results with those of previous studies, Tang et al. (2013) inverted CO  
707 emissions over Beijing and the surrounding areas and obtained comparable  
708 improvements (Table 6) in the RMSE (37–48% vs. 30–51%) and CORR (both studies  
709 ~ 0.81); however, we decreased the biases by 90–97%, which is much greater than their  
710 48–64% reductions. Additionally, Chen et al. (2019) showed that the RMSE of  
711 simulated SO<sub>2</sub> with updated SO<sub>2</sub> emissions decreased by 4.2–52.2% for different  
712 regions, and the CORR only increased to 0.69 at most. These improvements are smaller  
713 than those obtained in this study, which may be due to the insufficient adjustment of  
714 emissions caused by the underestimated ensemble spread through the inflation method.  
715 The better performance in this study may be related to our inversion process, which  
716 causes the optimized emissions of the current DA window to propagate to the next DA  
717 window for further correction.

718 **Table 6.** Statistics comparing the pollution concentrations from the simulations with  
 719 prior (CEP) and posterior (VEP) emissions against assimilated and independent  
 720 observations, respectively. CO unit: mg m<sup>-3</sup>; others units: µg m<sup>-3</sup>.

Species	Mean Obs.	Mean Sim.		BIAS		RMSE		CORR	
		CEP	VEP	CEP	VEP	CEP	VEP	CEP	VEP
Against assimilated observations									
CO	1.43	0.66	1.36	-0.77	-0.08	1.08	0.56	0.46	0.81
SO <sub>2</sub>	32.5	34.4	28.4	1.9	-4.1	42.4	17.7	0.39	0.88
NO <sub>2</sub>	43.8	40.8	39.0	-2.9	-4.8	25.0	12.3	0.65	0.88
PM <sub>2.5</sub>	77.0	53.1	70.3	-24.0	-6.7	50.3	29.6	0.64	0.87
PMC	40.5	8.1	37.5	-32.4	-3.1	41.5	24.6	0.25	0.69
Against independent observations									
CO	1.54	0.79	1.52	-0.75	-0.02	1.15	0.72	0.59	0.82
SO <sub>2</sub>	40.6	39.2	37.3	-1.3	-3.2	44.3	27.2	0.57	0.87
NO <sub>2</sub>	50.2	50.0	47.5	-0.3	-2.7	21.7	15.9	0.73	0.83
PM <sub>2.5</sub>	91.5	64.6	84.1	-26.9	-7.4	64.1	37.2	0.62	0.87
PMC	42.0	9.2	40.4	-32.8	-1.6	39.3	26.6	0.39	0.62

721 \* BIAS, mean bias; RMSE, root mean square error; CORR, correlation coefficient

#### 722 4.1.4 Uncertainty reduction

723 The uncertainty reduction rate (UR) is an important quantity to evaluate the  
 724 performance of RAPAS and the effectiveness of *in situ* observations (Chevallier et al.,  
 725 2007; Jiang et al., 2021; Takagi et al., 2011). Following Jiang et al. (2021), the UR was  
 726 calculated as

$$727 \quad UR = \left(1 - \frac{\sigma_{posterior}}{\sigma_{prior}}\right) \times 100 \quad (19)$$

728 where  $\sigma_{posterior}$  and  $\sigma_{prior}$  are the posterior and prior uncertainties, respectively,  
 729 calculated using the standard deviations of the prior and posterior perturbations (Text  
 730 S2). Table 7 shows the URs averaged in each province and mainland China. URs varied  
 731 with species as they are closely related to the magnitude settings of prior uncertainties  
 732 (Jiang et al., 2021). The URs of PPM<sub>2.5</sub> and PMC were the most effective while the UR  
 733 of NO<sub>x</sub> emissions was the lowest. For mainland China overall, uncertainties were  
 734 reduced by 44.4%, 45.0%, 34.3%, 51.8%, and 56.1% for CO, SO<sub>2</sub>, NO<sub>x</sub>, PPM<sub>2.5</sub>, and

735 PMC, respectively. For one species, URs varied across provinces. URs are usually  
 736 related to observation coverage, which means that the more observation constraints  
 737 there are, the more URs decrease. Additionally, URs may also be related to emission  
 738 distributions. Generally, URs were more significant in the provinces where  
 739 observations and emissions were both relatively concentrated (e.g. Tibet), while they  
 740 were much lower where the emissions were scattered or relatively uniform, but the  
 741 observations were only in large cities, even if there were many more observations than  
 742 in other provinces.

743 **Table 7.** Time-averaged posterior emission uncertainty reduction (%) indicated by the  
 744 standard deviation reduction of total emissions per province calculated by prior and  
 745 posterior ensembles.

Province	CO	SO <sub>2</sub>	NO <sub>x</sub>	PPM <sub>2.5</sub>	PMC
Mainland	44.4	45.0	34.3	51.8	56.1
Shanghai	16.9	16.7	20.8	24.7	18.5
Jiangsu	17.7	25.3	29.3	34.1	52.3
Zhejiang	24.7	13.3	17.9	42.4	31.4
Anhui	20.1	52.7	39.1	58.1	40.9
Shandong	32.1	30.0	20.3	53.7	26.7
Beijing	28.2	6.2	37.0	43.3	31.4
Tianjin	20.0	7.0	21.4	41.3	17.8
Hebei	29.5	40.2	28.8	56.0	30.3
Shanxi	38.4	37.9	22.5	55.3	35.0
Neimenggu	30.1	45.8	40.4	37.6	52.8
Henan	27.4	16.1	21.9	53.7	30.8
Hunan	36.0	27.7	34.4	16.9	41.6
Hubei	30.8	16.6	26.0	46.4	46.5
Jiangxi	20.9	28.4	29.4	47.0	46.7
Guangdong	31.2	14.9	41.1	53.1	46.4
Guangxi	22.6	13.9	42.5	48.1	55.2
Fujian	9.9	8.1	31.9	31.6	49.2
Hainan	0.6	0.5	4.5	0.7	23.3
Liaoning	35.6	34.6	19.0	33.9	54.0
Heilongjiang	29.9	27.7	17.4	42.0	65.2
Jilin	27.9	44.5	18.7	42.0	42.8
Shaanxi	41.3	13.2	29.8	47.9	43.1
Gansu	24.8	36.1	33.7	46.3	56.4
Xinjiang	38.3	27.9	20.2	46.3	66.5
Qinghai	53.9	25.8	27.3	46.0	57.9
Ningxia	47.0	36.6	17.6	38.0	30.1
Sichuan	29.4	25.0	39.5	61.1	46.5
Chongqing	5.7	8.2	8.8	12.7	13.8
Guizhou	14.4	16.4	26.6	40.3	38.2
Yunnan	38.3	29.9	31.4	40.1	55.9
Tibet	30.2	0.5	52.8	67.3	73.2

746

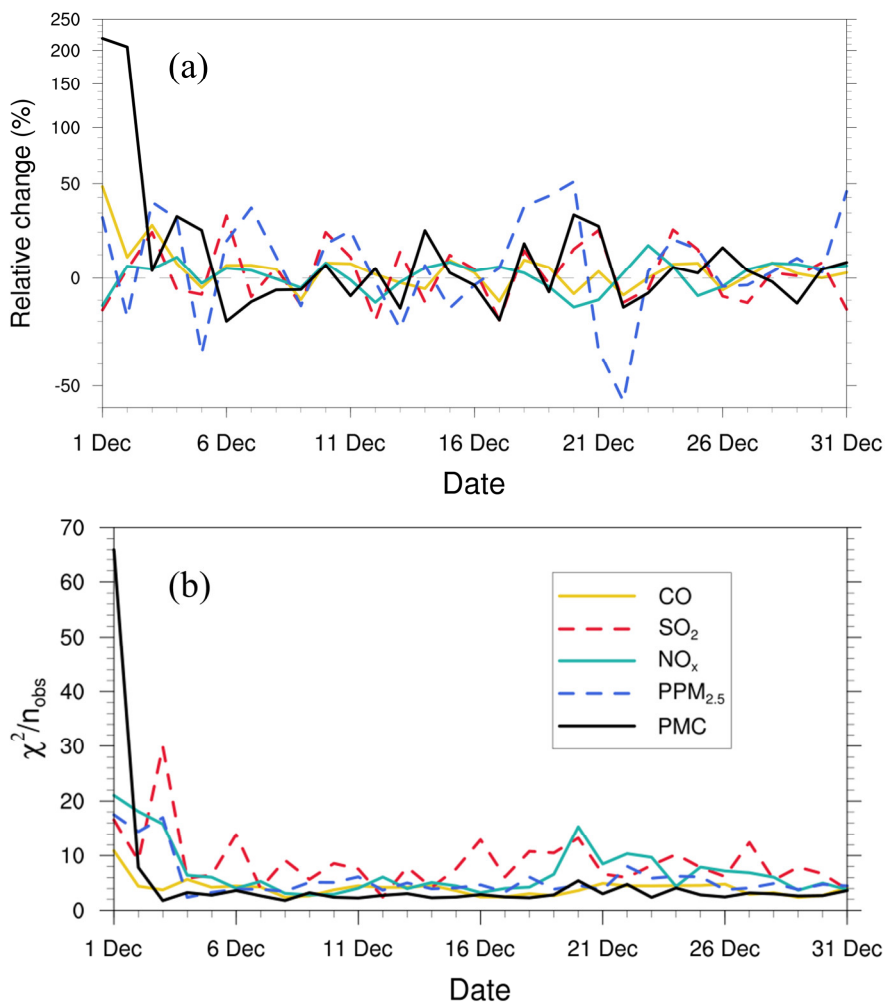
747 **4.1.5 Evaluation using chi-squared statistics**

748 To diagnose the performance of the EnKF analysis, chi-squared ( $\chi^2$ ) statistics were  
749 calculated, which are generally used to test whether the prior ensemble mean RMSE  
750 with respect to the observations is consistent with the prior “total spread” (square root  
751 of the sum of ensemble variance and observation error variance). Following Zhang et  
752 al. (2015), for the  $t$ th window,  $\chi^2$  is defined as:

$$753 \quad \chi_t^2 = (\mathbf{y} - \mathbf{H}\overline{\mathbf{X}}^b)^T (\mathbf{H}\mathbf{P}^b\mathbf{H}^T + \mathbf{R})^{-1} (\mathbf{y} - \mathbf{H}\overline{\mathbf{X}}^b) \quad (20)$$

754 Figure 9 shows the time series of the relative changes between the prior and posterior  
755 emissions and the  $\chi^2$  statistics. There were relatively large adjustments in emissions in  
756 the first three windows, especially for the PMC. Subsequently, the five species reached  
757 a more optimal state with successive emission inversion cycles. The  $\chi^2$  statistics showed  
758 similar variation characteristics as the daily changes in emissions. The  $\chi^2$  value was  
759 slightly greater than 1, indicating that the uncertainties from the error covariance  
760 statistics did not fully account for the error in the ensemble simulations. A similar result  
761 was reported by Chen et al. (2019). Further investigations should be conducted to  
762 generate larger spreads by accounting for the influence of model errors. As we imposed  
763 the same uncertainty of prior emissions at each DA window to partially compensate for  
764 the influence of model errors,  $\chi^2$  statistics showed small fluctuations, indicating that the  
765 system updated emissions consistently and stably.

766



767

768 **Figure 9.** Relative changes (a) in posterior emission estimates of CO, SO<sub>2</sub>, NO<sub>x</sub>, PPM<sub>2.5</sub>,  
 769 and PMC and  $\chi^2$  statistics (b) of these state vectors in each window.

#### 770 4.1.6 Evaluation using OSSE

771 Figure 10 shows the spatial distribution of the error reduction in the posterior emissions  
 772 of the five species. After inversion, in most areas, the emission errors were reduced by  
 773 more than 80%, especially in the central and eastern regions with dense observation  
 774 sites, while in remote areas far away from cities, due to the sparse observation sites, the  
 775 emission errors were still not well adjusted. Overall, the error reduction rates of CO,  
 776 SO<sub>2</sub>, NO<sub>x</sub>, PPM<sub>2.5</sub>, and PMC were 78.4%, 86.1%, 78.8%, 77.6%, and 72.0%,  
 777 respectively, indicating that with the *in situ* observations in China, RAPAS can  
 778 significantly reduce emission errors and thus showed good performance in emission  
 779 estimates.

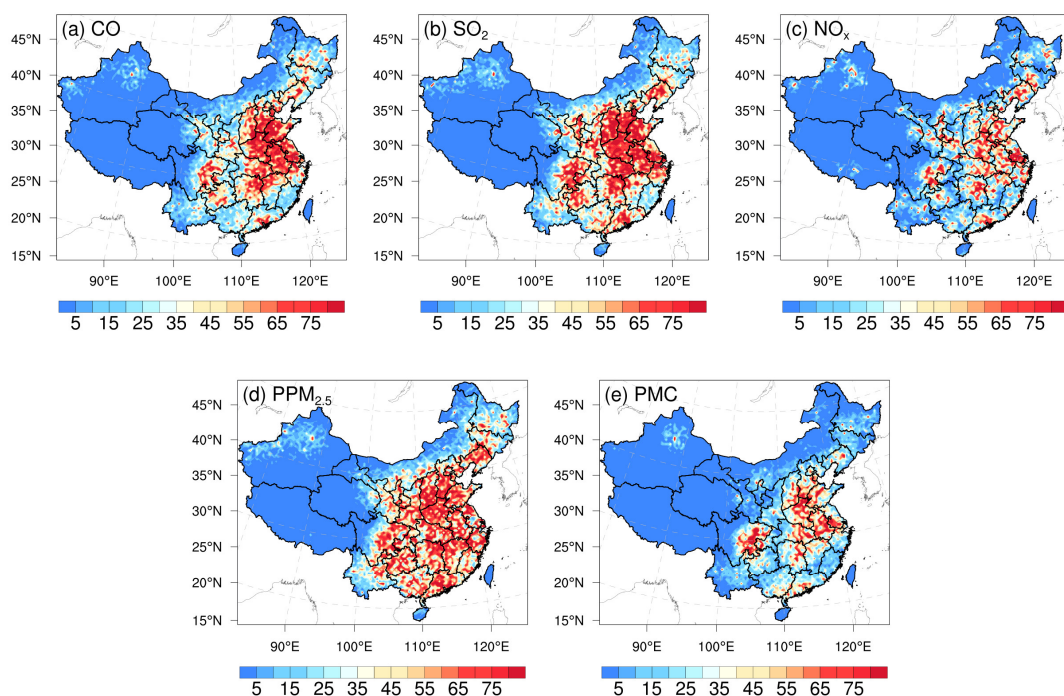


**Figure 10.** Spatial distribution of the error reduction (%) of posterior emissions in the OSSE.

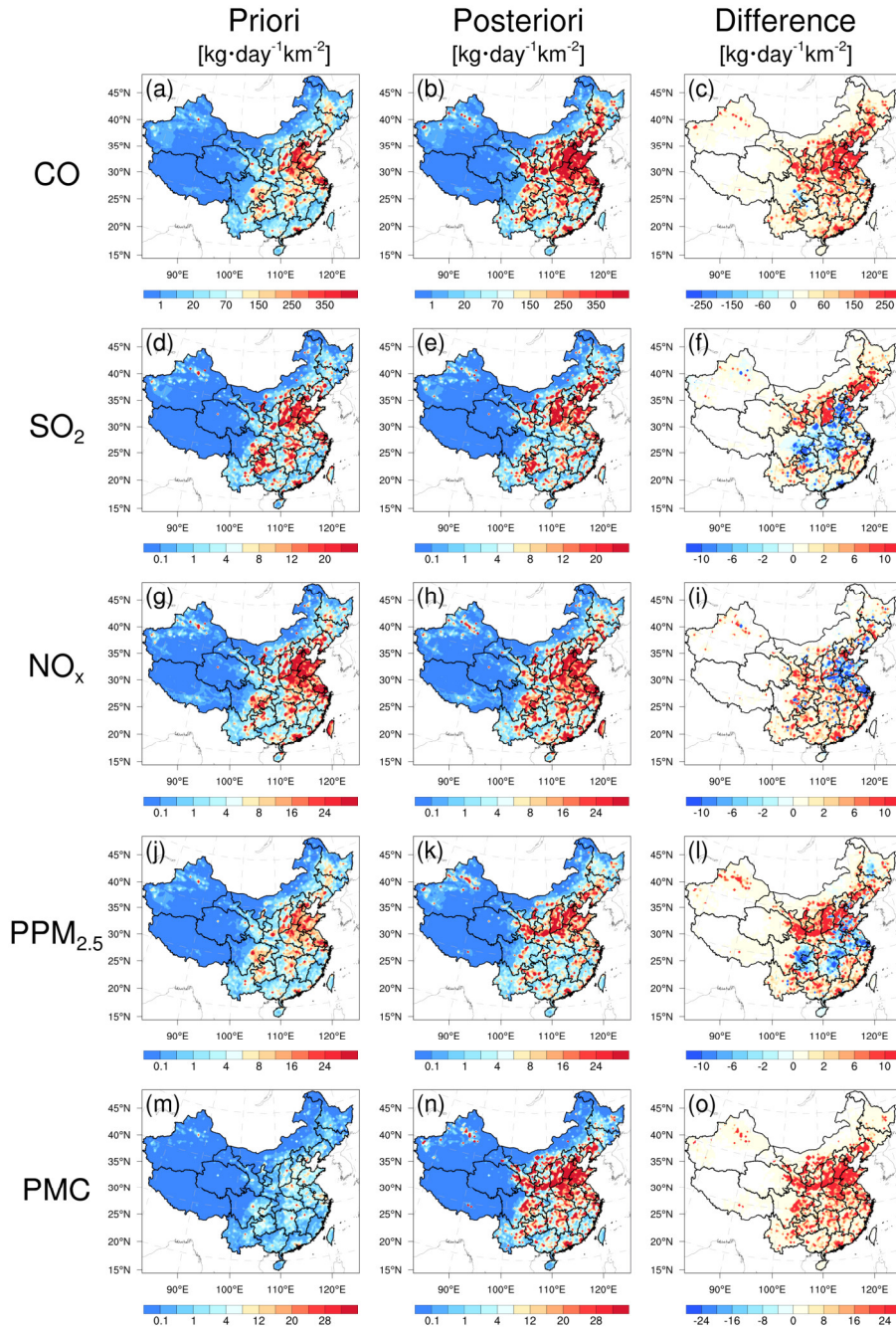
#### 4.2 Inverted emissions

Figure 11 shows the spatial distribution of temporally averaged prior and posterior emissions and their differences in emissions in December 2016. It should be noted that emissions outside China were masked; as the observation sites were limited to China in this study, there was a slight change in the emissions outside China. Higher emissions were mainly concentrated in central and eastern China, especially in the NCP, YRD, and PRD, and lower emissions occurred across Northwest and Southern China. Compared with the prior emissions, posterior CO emissions were considerably increased across most areas of mainland China, especially in northern China, with an overall increase of 129%. A notable underestimation of prior emissions was also confirmed by inversion estimations (Feng et al., 2020b; Tang et al., 2013; Wu et al., 2020) and model evaluations (Kong et al., 2019b) in previous studies. For SO<sub>2</sub>, the emissions increased mainly in Northeast China, Shanxi, Ningxia, Gansu, Fujian, Jiangxi, and Yunnan provinces. In SCB, Central China, YRD, and part of the NCP,

Please spell out

797 emissions were significantly reduced. The national total SO<sub>2</sub> emissions increased by  
798 20%. For NO<sub>x</sub>, although the increment of national total emissions was small  
799 (approximately 5%), there were large deviations. The emissions in NCP and YRD were  
800 reduced, whereas the emissions in most cities in other regions increased. The changes  
801 in the emission of PPM<sub>2.5</sub> were similar to those of SO<sub>2</sub>. Compared with the prior  
802 emissions, the posterior PPM<sub>2.5</sub> emissions decreased over central China, SCB, and YRD,  
803 whereas those in southern and northern China increased, especially in Shanxi, Shaanxi,  
804 Gansu, and southern Hebei provinces. Overall, the relative increase was 95%. For PMC,  
805 the posterior emissions were increased over all of mainland China, with national mean  
806 relative increase exceeding 1000%. Larger emission increments mainly occurred in  
807 areas with significant anthropogenic emissions of CO and PPM<sub>2.5</sub>, indicating that the  
808 large underestimation of PMC emissions in the prior inventory may be mainly  
809 attributed to the underestimations of anthropogenic activities. The absence of natural  
810 dust is another reason, as the wind-blown dust scheme was not applied in this study.  
811 Overall, PM<sub>10</sub> emissions (PPM<sub>2.5</sub>+PMC) increased by 318%. If we assume that all the  
812 increments in PM<sub>10</sub> emissions are from natural dust, that means the contribution of  
813 natural dust accounted for 75% of total PM<sub>10</sub> emissions, which is consistent with the  
814 source apportionment of PM<sub>10</sub> of 75% in Changsha in Central China (Li et al., 2010).  
815 Large PMC emission increments were also reported by Ma et al. (2019).

816 Detailed estimations of posterior emissions and relative changes compared to prior  
817 emissions in each province and mainland China are given in Table S1. The evaluation  
818 results for July showed that the emission uncertainty could still be significantly reduced  
819 and the performance of the system in July was comparable to that in December (Table  
820 S2). Additionally, the seasonal variation in emissions was well reflected (Figures S4  
821 and S5), which means that our system performed well at different times of the year.  
822 Note that the differences, excluding PMC, between the prior and posterior emissions  
823 mainly reflect the deficiencies of the prior emissions as the times of the prior emissions  
824 and observations were consistent in this study.



825

826 **Figure 11.** Spatial distribution of the time-averaged prior emissions (left column, MEIC  
 827 2016), posterior emissions (middle column), and differences (right column, posterior  
 828 minus prior).

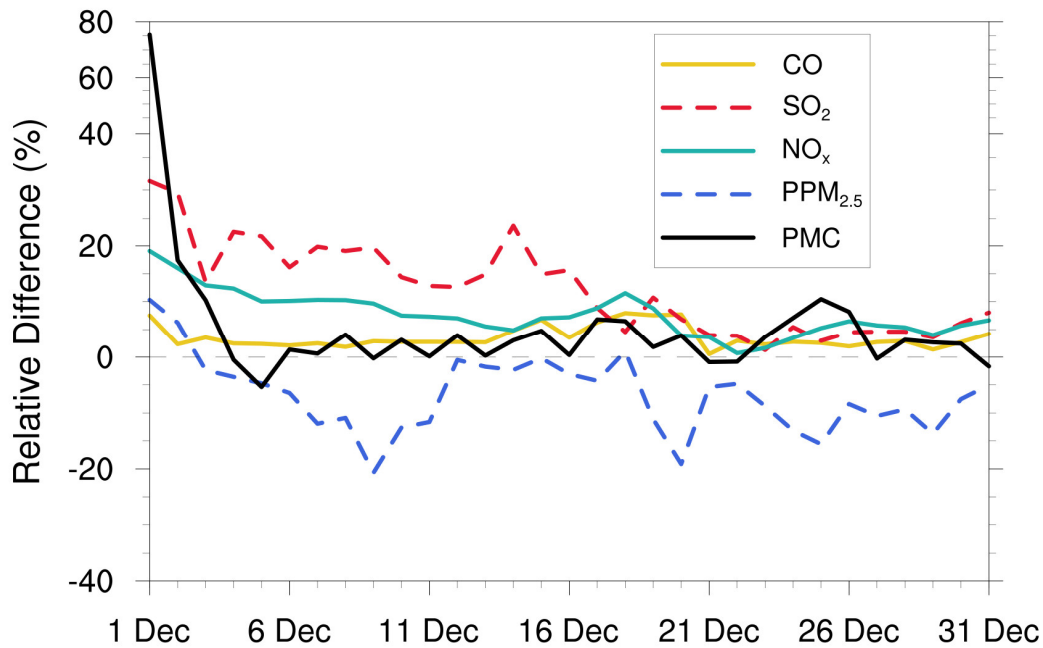
### 829 4.3 Sensitivity tests

#### 830 4.3.1 Impact of prior inventories

831 Various prior inventories have shown considerable differences in space allocation and



832 emission magnitudes. Inversion results can be sensitive to a priori emissions if the  
833 observations are insufficient (Gurney et al., 2004; He et al., 2018). MEIC 2012 was  
834 used as an alternative a priori in EMS1 to investigate the impact of different prior  
835 emissions on posterior emissions. Figure 12 shows the time series of the relative  
836 differences in the daily posterior emissions of the five species between the EMDA (base)  
837 and EMS1 experiments. Overall, the differences between the two posterior emissions  
838 gradually decreased over time. At the beginning, the differences in the CO, SO<sub>2</sub>, NO<sub>x</sub>,  
839 PPM<sub>2.5</sub>, and PMC between the two inventories (i.e. MEIC 2012 vs. MEIC 2016) were  
840 17.5%, 114.5%, 30.8%, 46.0%, and 72.0%, respectively, compared to 2.5%, 4.5%,  
841 4.5%, -8.9%, and 3.0% in the last ten days. In addition, the species with larger emission  
842 differences at the beginning took a longer time (i.e. more DA steps) to achieve  
843 convergence. The quick convergence of PMC emissions was attributed to the large prior  
844 uncertainty of 100% used in the first three DA windows. In contrast to the other species,  
845 there were significant negative deviations in PPM<sub>2.5</sub> emissions between the two  
846 experiments. This may be due to the positive deviations in the precursors of PM<sub>2.5</sub> (i.e.,  
847 SO<sub>2</sub> and NO<sub>x</sub>), which lead to a larger amount of secondary production. The PPM<sub>2.5</sub>  
848 emissions will be reduced to balance the total PM<sub>2.5</sub>. We compared the PM<sub>2.5</sub>  
849 concentrations simulated by the two optimized inventories and found that they were  
850 almost the same (Figure S6). Overall, this indicates that observations in China were  
851 sufficient to infer emissions and that our system was robust. Meanwhile, the monthly  
852 posterior emissions shown in Section 4.2 were still underestimated to a certain extent.



853

854 **Figure 12.** Relative differences in CO, SO<sub>2</sub>, NO<sub>x</sub>, PPM<sub>2.5</sub>, and PMC emissions (% the  
 855 ratio of absolute difference to EMDA) between the EMDA and EMS1 experiments.

856

### 857 4.3.2 Impact of prior uncertainties settings

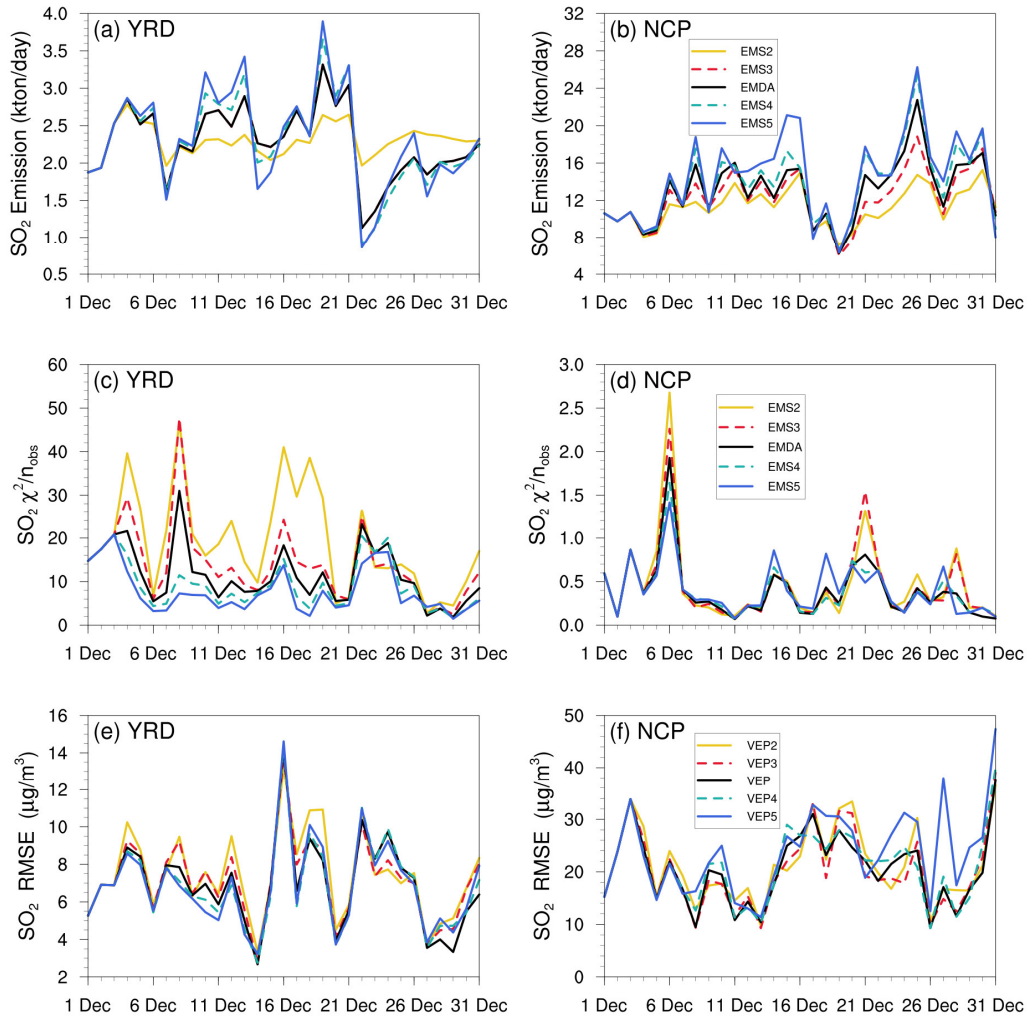
858 The uncertainty of prior emissions determines how closely the analysis is weighted  
 859 towards the background and observations; however, information about prior  
 860 uncertainties is generally not readily available. To evaluate the possible influence of  
 861 prior uncertainties on the optimized emissions, we increased/reduced the uncertainties  
 862 after three days of cycling, namely starting at 0000 UTC, 3 December, by 25% and 50 %  
 863 in EMS2 (-50%), EMS3 (-25%), EMS4 (+25%), and EMS5 (+50%), respectively. Table  
 864 8 summarizes the emission changes with different prior uncertainty settings in the  
 865 EMS2–5 experiments. To better understand the response of the system to the emission  
 866 uncertainty settings, Figure 13 illustrates the time series of SO<sub>2</sub> emission changes, Chi-  
 867 square statistics, and RMSEs of simulated SO<sub>2</sub> with emissions updated in the EMDA  
 868 and EMS2–5 experiments over the YRD and NCP (Figure 2). Compared with the  
 869 EMDA, when the uncertainties decreased (increased), the emissions of the five species  
 870 decreased (increased) accordingly. This is because the posterior emissions of the five  
 871 species were larger than the prior emissions and, as shown in Figure 13a–d, larger

872 uncertainty will lead to faster convergence, resulting in larger posterior emissions. It  
873 can also be seen from Figure 13 that a faster convergence will reduce the RMSE of the  
874 simulated concentration with the posterior emissions in the early stage of the  
875 experiment; however, in the later stage of the experiment, there were no significant  
876 differences in the RMSE and Chi-square statistics among the different experiments.  
877 However, day-to-day changes in emissions also cause slight fluctuations. In addition,  
878 when greater uncertainties are set, the day-to-day changes in emissions are more drastic,  
879 resulting in a larger RMSE, as shown in the NCP. Moreover, the significant day-to-day  
880 variations in the estimated emissions may not be in line with the actual situation. Owing  
881 to the spatial-temporal inhomogeneity of emissions, the differences in Chi-square  
882 statistics between the YRD and NCP show that it may be necessary to apply different a  
883 priori uncertainties according to different regions (Chen et al., 2019). Therefore, when  
884 using an EnKF system for emission estimation, error setting must be carefully executed.  
885 Overall, the uncertainties chosen in EMDA aim to minimize the deviation of the  
886 concentration fields and maintain the stability of the inversion.

887 **Table 8.** Relative differences in CO, SO<sub>2</sub>, NO<sub>x</sub>, PPM<sub>2.5</sub> and PMC emissions (% , the  
888 ratio of absolute difference to EMDA) between the EMDA and EMS2-5 experiments.

Species	EMS2	EMS3	EMS4	EMS5
CO	-8.6	-4	3	5.2
SO <sub>2</sub>	-14	-5.7	3.6	6.8
NO <sub>x</sub>	-6.5	-3	2.8	4.5
PPM <sub>2.5</sub>	-16.5	-7.8	4.6	8.7
PMC	-18.5	-8.2	7.3	13.1

889



890

891 **Figure 13.** Time-series of SO<sub>2</sub> emission changes, Chi-square statistics, and RMSE of  
 892 simulated SO<sub>2</sub> with updated SO<sub>2</sub> emissions in the EMDA and EMS2-5 experiments  
 893 over the YRD and NCP.

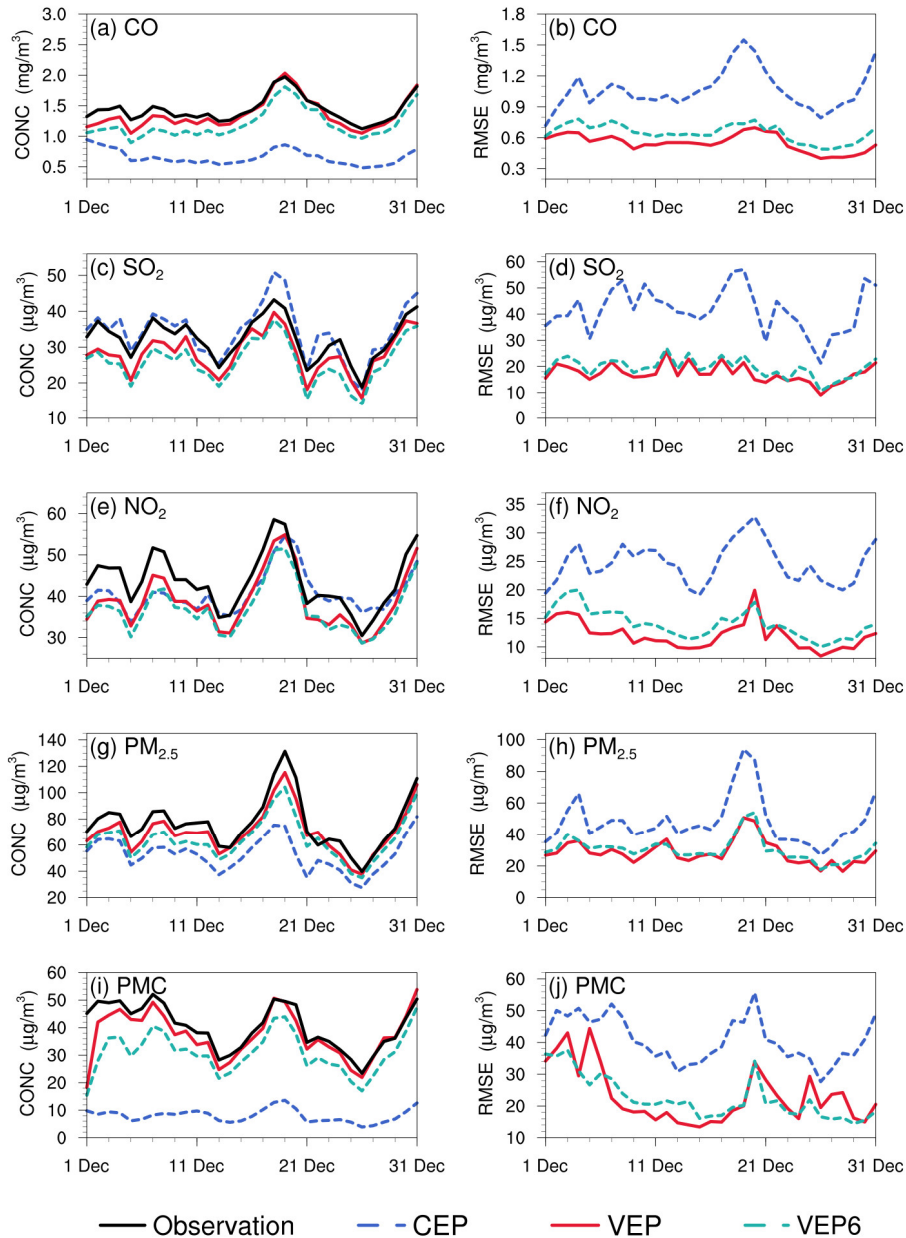
### 894 4.3.3 Impact of observation error settings

895 Observation errors are another factor that determine the relative weights of the  
 896 observations and background in the analysis. A proper estimate of the observation error  
 897 is important for filter performance; however, observation errors are generally not  
 898 provided with datasets. The observation error is usually set to a fixed value (Ma et al.,  
 899 2019), specific proportion of the observation value (Tang et al., 2013), or value  
 900 calculated by combining measurement error with representative error as used in this  
 901 study. Generally, the performance of data assimilation is sensitive to the specification

A sensitivity ...

8

902 of the observation error (Tang et al., 2013). Sensitivity experiment (EMS6) with  
903 doubled observation error was conducted to evaluate the influence of observation error  
904 on the optimized emissions. Overall, the spatial distribution of emissions after  
905 optimization was almost the same as that of the EMDA experiment but with a lower  
906 increment (Figure S7), resulting in a weaker estimate of the national total emissions for  
907 each species. This is because that the observation error inflates and the system becomes  
908 more certain of the prior emission, and reduces the effect of observation information.  
909 Figure 14 shows the time series of simulated and observed daily concentrations and  
910 their RMSEs verified against the assimilated sites. The simulations in VEP6 usually  
911 performed worse, with larger biases and RMSEs than those of VEP (Figures S8 and S9),  
912 especially in western and southern China, where posterior emissions were significantly  
913 underestimated. These results generally corresponded to sluggish emission changes and  
914 large Chi-square statistics (Figure S10), suggesting that an observation error that is too  
915 large may substantially impact the estimated emissions.



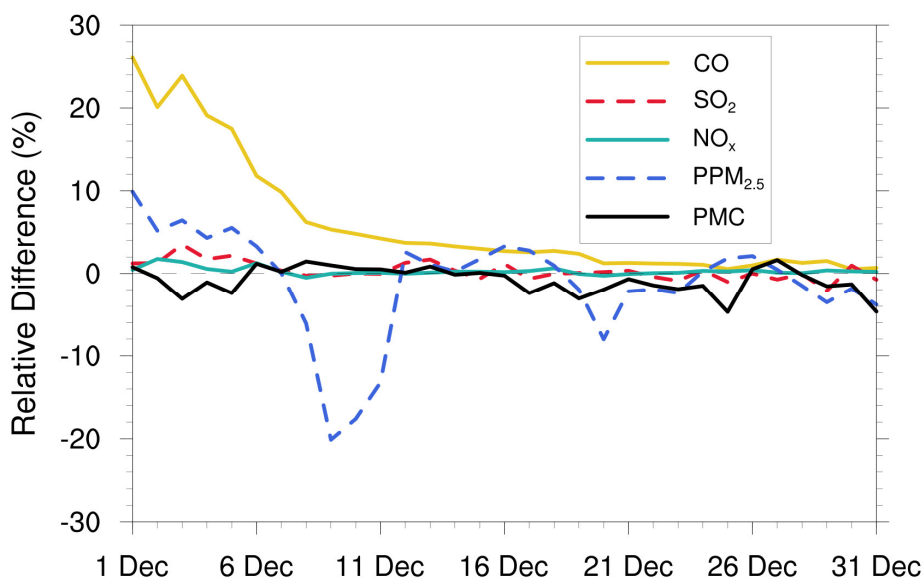
916

917 **Figure 14.** Time series of the daily concentrations (CONC, left) and root mean square  
 918 error (RMSE, right) obtained from CEP, VEP, and VEP7. The simulations were verified  
 919 against the assimilated sites.

#### 920 4.3.4 Impact of the IC optimization of the first window

921 Several studies indicate large emission discrepancies resulting from IC errors (Jiang et  
 922 al., 2013a; Miyazaki et al., 2017; Tang et al., 2013), which means that if the IC is not  
 923 optimized, the errors of concentrations would be compensated for through the  
 924 adjustment of emissions. To evaluate the impact of IC optimization of the first window

925 on the emission inversions, an EMS7 experiment without the IA step was conducted.  
 926 Figure 15 shows the time series of the relative differences in the daily posterior  
 927 emissions of the five species between the EMDA and EMS7 experiments. It can be  
 928 observed that IC optimization had a significant impact on the emission inversions of  
 929 long-lived species (i.e. CO). The overall difference in the inverted CO emissions  
 930 between the two experiments was approximately 5.3% but can reach 26.1% in the first  
 931 few windows. For the short-lived species, IC optimization had little impact on the  
 932 emissions; for example, the average emission differences of SO<sub>2</sub>, NO<sub>x</sub>, and PMC in the  
 933 two experiments were 0.3%, 0.3%, and 0.9%, respectively. For PPM<sub>2.5</sub>, the average  
 934 emission difference is affected not only by primary emissions, but also by the complex  
 935 chemistry of its precursors. Therefore, the difference between the two experiments  
 936 fluctuated, with overall difference of 2%. Notably, with the gradual disappearance of  
 937 the benefit of IC assimilation, the two experiments reached a unified state after several  
 938 windows. For CO, the impact of IA on emission inversion lasted approximately half a  
 939 month. These results indicate that removing the bias of the IC of the first DA window  
 940 is essential for the subsequent inverse analysis (Jiang et al., 2017).



941

942 **Figure 15.** Relative differences in CO, SO<sub>2</sub>, NO<sub>x</sub>, PPM<sub>2.5</sub>, and PMC emissions (% the  
 943 ratio of absolute difference to EMDA) between the EMDA and EMS7.

#### 944 **4.4 Discussion**

945 Optimal state estimation using an EnKF relies on the assumption of an unbiased  
946 Gaussian prior error, which is not guaranteed in such highly nonlinear and large bias  
947 systems. In this study, some pollutants (e.g. CO, PMC) have very large simulated biases;  
948 thus, if a small uncertainty is adopted, the emission bias cannot be fully reduced. If a  
949 very large uncertainty is adopted, then the degree of freedom of adjustment is too large  
950 and the inverted daily emissions will fluctuate abnormally. Therefore, we only set a  
951 larger prior uncertainty in the first three windows, adopting a moderate uncertainty in  
952 the following windows and used a “two-step” inversion scheme and cyclic iteration to  
953 gradually correct the emission errors. Figure 9a shows the time series of the relative  
954 differences between prior and posterior emissions in each window. There were  
955 relatively large adjustments for the emissions in the first three windows, especially for  
956 PMC, but the adjustment ranges of the five species after the first three windows were  
957 within the uncertainty range (e.g.  $\pm 25\%$ ), indicating that with this scheme, the EnKF  
958 method used in this system had a good performance in emission inversion.

959 Model-data mismatch errors are from both the emissions and the inherent model errors  
960 arising from the model structure, discretization, parameterizations, and biases in the  
961 simulated meteorological fields. Neglecting model errors would attribute all  
962 uncertainties to emissions and lead to considerable bias in the estimated emissions. In  
963 the version of the CMAQ model used in this study, there are no heterogeneous reactions  
964 (Quan et al., 2015; Wang et al., 2017), the parameterization scheme for the formation  
965 of secondary organic aerosols (SOA) is imperfect (Carlton et al., 2008; Jiang et al.,  
966 2012; Yang et al., 2019), no feedback between chemistry and meteorology was  
967 considered, and we used an idea profile for chemical lateral boundary conditions. All  
968 the above problems can lead to underestimated concentrations of pollutants, which in  
969 turn require more emissions to compensate, leading to overestimation of emissions. In  
970 addition, previous studies showed that ammonia emissions in the MEIC inventory are  
971 underestimated (Kong et al., 2019b; Paulot et al., 2014; Zhang et al., 2018). Owing to  
972 lack of ammonia observations, our system does not include emission estimates of



973 ammonia, which means that the concentration of ammonium aerosol was  
974 underestimated in this system, also resulting in an overestimation of the PPM<sub>2.5</sub>  
975 emission. Wind-blown dust was also not simulated; thus, the PMC emission inverted in  
976 this system come from anthropogenic activities and natural sources. Although some of  
977 these shortcomings can be solved by updating the CTM model, there will still be errors  
978 in each parameterization and process. In general, a parameter estimation method was  
979 used to reduce the model errors, in which some uncertain parameters were included in  
980 the augmented state vector and optimized synchronously based on the available  
981 observations (Brandhorst et al., 2017; Evensen, 2009). However, it is difficult to  
982 identify the key uncertain parameters of different species in different models, which  
983 generally comes not only from the complex atmospheric chemical model but also from  
984 hundreds of model inputs (Tang et al., 2013). Another method is bias correction, which  
985 treats the model error as a bias term and includes it in an augmented state vector  
986 (Brandhorst et al., 2017; De Lannoy et al., 2007; Keppenne et al., 2005). In addition,  
987 the weak-constraint 4DVAR method can be used to reduce model errors, which adds a  
988 correction term in the model integration to account for the different sources of model  
989 error (Sasaki, 1970). Although the reliable diagnosis of model error remains a challenge  
990 (Laloyaux et al., 2020), it should be considered in an assimilation system. In the future,  
991 we will consider model errors in our system to obtain better emission estimates.

992 Independent variable localization was adopted to avoid potential spurious correlations  
993 across different species in this study. However, the transmission scales for different  
994 species in different regions differ, and a more accurate localization range can be  
995 obtained through backward trajectory analysis. In addition, O<sub>3</sub> observations were not  
996 assimilated to improve NO<sub>x</sub> and VOC emissions using cross-species information. O<sub>3</sub>  
997 concentration and NO<sub>x</sub> (VOC) emissions were positively correlated in the NO<sub>x</sub> (VOC)-  
998 limited region and negatively correlated in the VOC (NO<sub>x</sub>)-limited region (Tang et al.,  
999 2011; Wang et al., 2019b). Hamer et al. (2015) successfully used O<sub>3</sub> observations to  
1000 estimate NO<sub>x</sub> and VOC emissions within the 4DVAR framework within an ideal model.  
1001 However, the NO<sub>x</sub> emissions are often point or line sources, which are all small

1002 compared to the model resolution. With a coarse spatial resolution, the model cannot  
1003 accurately simulate the relationships between O<sub>3</sub> and its precursors. When assimilating  
1004 O<sub>3</sub> observations to infer NO<sub>x</sub> or VOC emissions, the inaccurate relationships simulated  
1005 by model would worsen the inversion of NO<sub>x</sub> emissions (Inness et al., 2015). In general,  
1006 improving the model resolution can improve the detailed simulation and provide better  
1007 prior information on O<sub>3</sub>-NO<sub>x</sub>-VOC, but it is still difficult to determine whether the  
1008 condition is NO<sub>x</sub>-limited or VOC-limited in the real atmosphere using prior emissions  
1009 (Liu and Shi, 2021). Elbern et al. (2007) emphasized that assimilating O<sub>3</sub> to correct NO<sub>x</sub>  
1010 or VOC emissions must follow the EKMA framework derived based on observations,  
1011 otherwise, even if the resolution is improved to sufficiently solve point and line sources,  
1012 precursor emissions may be still adjusted in an opposite direction. This can be  
1013 demonstrated in our OSSE experiment at high resolution of 3 km (Figure S11). In this  
1014 study, the spatial resolutions of the prior emission inventory (i.e., MEIC) is 0.25° ×  
1015 0.25°, which is appropriate for modeling at regional scales (Zheng et al., 2017). With  
1016 this emission inventory, it is unable to accurately simulate the O<sub>3</sub>-NO<sub>x</sub>-VOC  
1017 relationships. Therefore, to avoid the impact of inaccurate O<sub>3</sub>-NO<sub>x</sub> relationship on  
1018 emission inversion, in our system, we did not assimilate O<sub>3</sub>, but directly assimilate NO<sub>2</sub>  
1019 to optimize the NO<sub>x</sub> emissions. This work will be followed by an ongoing study using  
1020 the available VOC observations.

1021 Although we do not assimilate O<sub>3</sub> observation, model resolution still has some influence  
1022 on inversion results. In our previous study (Feng et al., 2022), we have inferred the NO<sub>x</sub>  
1023 emissions over YRD in China using NO<sub>2</sub> observations, which has a spatial resolution  
1024 of 12 km. The study period, assimilated observations, and inversion settings are the  
1025 same as this study. We compared the posterior emissions of YRD between this study  
1026 and Feng et al. (2022). The results showed that there was similar spatial distribution of  
1027 posterior emissions inferred using the two resolutions (36 km vs 12 km) (Figure S12),  
1028 but the total NO<sub>x</sub> emission in YRD inferred using 36 km resolution was about 8.8%  
1029 higher than that inferred using 12 km resolution. The differences are mainly caused by  
1030 meteorological differences at different resolutions. This indicates that coarse model

1031 resolution may lead to some overestimation of the inverted emissions. In addition, as  
1032 shown previously, the concentrations after DA were evidently underestimated in  
1033 western China, indicating that the inverted emissions over these regions still have large  
1034 uncertainties because of the sparsity of observations, which are spatially insufficient for  
1035 sampling the inhomogeneity of emissions. Therefore, further investigations with the  
1036 joint assimilation of multisource observations (e.g. satellite) are underway.

1037 NO<sub>x</sub> is mainly emitted by transportation (Li et al., 2017), which can reflect the level of  
1038 economic activity to a certain extent. Weekly emission changes were explored to verify  
1039 the performance of the system in depicting emission changes (Figure S13). Although  
1040 the “weekend effect” of emissions in China is not significant (Wang et al., 2014; Wang  
1041 et al., 2015), the posterior NO<sub>x</sub> emission changes are in good agreement with the  
1042 observations. In our previous studies (Feng et al., 2020a; Feng et al., 2020b), this system  
1043 was successfully applied to optimize NO<sub>x</sub> and CO emissions. The inverted emission  
1044 changes were also in line with the epidemic control time points. Additionally, the  
1045 emission changes can reflect the emission migration from developed or urban areas to  
1046 developing or surrounding areas in recent years, which is consistent with the emission  
1047 control strategies in China. Although the system did not consider the model error,  
1048 resulting in a certain difference between the posterior and actual emissions, the  
1049 spatiotemporal changes in posterior emissions were relatively reasonable and can be  
1050 used to monitor emission changes and inform emission regulations.

## 1051 **5 Summary and conclusions**

1052 In this study, we developed a Regional multi-Air Pollutant Assimilation System  
1053 (RAPASv1.0) based on the WRF/CMAQ model, 3DVAR algorithm, and EnKF  
1054 algorithm. RAPAS can quantitatively optimize gridded emissions of CO, SO<sub>2</sub>, NO<sub>x</sub>,  
1055 PPM<sub>2.5</sub>, and PMC on a regional scale by simultaneously assimilating hourly *in situ*  
1056 measurements of CO, SO<sub>2</sub>, NO<sub>2</sub>, PM<sub>2.5</sub>, and PM<sub>10</sub>. This system includes two subsystems:  
1057 IA subsystem and EI subsystem, which optimize chemical ICs and infer anthropogenic  
1058 emissions.

1059 Taking the 2016 MEIC in December as a priori, the emissions of CO, SO<sub>2</sub>, NO<sub>x</sub>, PPM<sub>2.5</sub>,  
1060 and PMC in December 2016 were inferred by assimilating the corresponding  
1061 nationwide observations over China. The optimized ICs and posterior emissions were  
1062 examined against assimilated and independent observations through parallel forward  
1063 simulation experiments with and without DA. Sensitivity tests were performed to  
1064 investigate the impact of different inversion processes, prior emissions, prior  
1065 uncertainties, and observation errors on emission estimates.

1066 RAPAS showed a good performance in assimilating surface *in situ* observations, with  
1067 the calculated emission uncertainties reduced by 44.4%, 45.0%, 34.3%, 51.8%, and  
1068 56.1% for CO, SO<sub>2</sub>, NO<sub>x</sub>, PPM<sub>2.5</sub>, and PMC, respectively. It can also significantly  
1069 improve the simulations; the RMSEs of the simulated concentrations with posterior  
1070 emissions decreased by 40.1–56.3% and the CORRs increased from 0.26–0.66 to 0.69–  
1071 0.87 for different species. The OSSE experiment showed that the errors of posterior CO,  
1072 SO<sub>2</sub>, NO<sub>x</sub>, PPM<sub>2.5</sub>, and PMC could be reduced by 78.4%, 86.1%, 78.8%, 77.6%, and  
1073 72.0%, respectively. Overall, compared with the prior emissions (MEIC 2016), the  
1074 posterior emissions increased by 129%, 20%, 5%, and 95% for CO, SO<sub>2</sub>, NO<sub>x</sub>, and  
1075 PPM<sub>2.5</sub>, respectively. The posterior PMC emissions, which included anthropogenic and  
1076 natural dust contributions, increased by 1045%. Sensitivity tests with different prior  
1077 inventories showed that the observations in China were sufficient to infer emission and  
1078 that our system was less dependent on prior inventories. Additionally, sensitivity tests  
1079 with different prior uncertainties indicated that when the posterior emissions were  
1080 larger than the prior emissions, the emissions decreased/increased with  
1081 decreases/increases in uncertainties because of the different convergence rates. These  
1082 results demonstrate the advantage of the two-step method in emission inversion in that  
1083 the inversion errors of the last window can be transferred to the current window for  
1084 further optimization and robustness of the emissions estimated from RAPAS using  
1085 nationwide observations over China. It should be noted that the system usually responds  
1086 slowly to too small a priori uncertainties or too large observation errors, which may  
1087 result in large errors in the estimated emissions.

It seems that this number is not mentioned only in abstract and conclusion in the body of the article

1088 In summary, the comprehensive evaluation and sensitivity tests revealed that RAPAS  
1089 could serve as a useful tool for accurately quantifying the spatial and temporal changes  
1090 in multi-species emissions at regional scales and near-real time, which will be helpful  
1091 for air pollution control in China and other regions around the world with dense ground  
1092 observation networks.

1093

#### 1094 **Code and data availability**

1095 The codes of RAPAS v1.0 are available at <https://doi.org/10.5281/zenodo.5566225>.  
1096 The WRF model code is open-source code and can be obtained from the WRF Model  
1097 User's Page (<https://www2.mmm.ucar.edu/wrf/users>, last access: 25 April 2021). The  
1098 CMAQ model is available through an open license as well (<https://www.epa.gov/cmaq>,  
1099 last access: 25 April 2021). The observational and emission data used in this study are  
1100 available at <https://doi.org/10.5281/zenodo.4718290> (Feng and Jiang, 2021).

1101

#### 1102 **Author contribution**

1103 SF, FJ, ZW and ZJ developed RAPAS v1.0. SF and FJ designed the research. SF  
1104 performed model simulations, analyzed data, and prepared the paper with contributions  
1105 from all co-authors. FJ supervised the model development project and assisted in  
1106 conceptualization and writing. HW, WH, YS, LZ, YZ, CL, and WJ contributed to the  
1107 discussion and improvement of the paper.

1108

#### 1109 **Competing interests**

1110 The authors declare that they have no conflict of interest.

1111

1112

## 1113 **Acknowledgements**

1114 This work is supported by the National Key R&D Program of China (Grant No.  
1115 2020YFA0607504), the National Natural Science Foundation of China (Grant No.  
1116 41907378), and the Nanjing University Innovation and Creative Program for Ph.D.  
1117 candidate (Grant No. CXCY19-60). We are grateful to the High Performance  
1118 Computing Center (HPCC) of Nanjing University for doing the numerical calculations  
1119 in this paper on its blade cluster system, and thank the MEIC team for providing the  
1120 prior anthropogenic emissions (<http://www.meicmodel.org/>).

1121

## 1122 **References**

1123 Appel, K. W., Pouliot, G. A., Simon, H., Sarwar, G., Pye, H. O. T., Napelenok, S. L., Akhtar, F., and  
1124 Roselle, S. J.: Evaluation of dust and trace metal estimates from the Community Multiscale Air  
1125 Quality (CMAQ) model version 5.0, *Geoscientific Model Development*, 6, 883-899,  
1126 10.5194/gmd-6-883-2013, 2013.

1127 Alexe, M., Bergamaschi, P., Segers, A., Detmers, R., Butz, A., Hasekamp, O., Guerlet, S., Parker,  
1128 R., Boesch, H., Frankenberg, C., Scheepmaker, R. A., Dlugokencky, E., Sweeney, C., Wofsy,  
1129 S. C., and Kort, E. A.: Inverse modelling of CH<sub>4</sub> emissions for 2010-2011 using different  
1130 satellite retrieval products from GOSAT and SCIAMACHY, *Atmospheric Chemistry and  
1131 Physics*, 15, 113-133, 2015.

1132 Barbu, A. L., Segers, A. J., Schaap, M., Heemink, A. W., and Builtjes, P. J. H.: A multi-component  
1133 data assimilation experiment directed to sulphur dioxide and sulphate over Europe,  
1134 *Atmospheric Environment*, 43, 1622-1631, 2009.

1135 Bocquet, M.: Parameter-field estimation for atmospheric dispersion: application to the Chernobyl  
1136 accident using 4D-Var, *Quarterly Journal of the Royal Meteorological Society*, 138, 664-681,  
1137 2012.

1138 Bocquet, M., Elbern, H., Eskes, H., Hirtl, M., Žabkar, R., Carmichael, G. R., Flemming, J., Inness,  
1139 A., Pagowski, M., Pérez Camaño, J. L., Saide, P. E., San Jose, R., Sofiev, M., Vira, J., Baklanov,  
1140 A., Carnevale, C., Grell, G., and Seigneur, C.: Data assimilation in atmospheric chemistry  
1141 models: current status and future prospects for coupled chemistry meteorology models,  
1142 *Atmospheric Chemistry and Physics*, 15, 5325-5358, 2015.

1143 Bocquet, M. and Sakov, P.: Joint state and parameter estimation with an iterative ensemble Kalman  
1144 smoother, *Nonlinear Processes in Geophysics*, 20, 803-818, 2013.

1145 Basu, S., Guerlet, S., Butz, A., Houweling, S., Hasekamp, O., Aben, I., Krummel, P., Steele, P.,  
1146 Langenfelds, R., Torn, M., Biraud, S., Stephens, B., Andrews, A., and Worthy, D.: Global CO<sub>2</sub>  
1147 fluxes estimated from GOSAT retrievals of total column CO<sub>2</sub>, *Atmospheric Chemistry and*

1148 Physics, 13, 8695-8717, 2013.

1149 Bauwens, M., Compornolle, S., Stavrakou, T., Müller, J.-F., van Gent, J., Eskes, H., Levelt, P. F.,  
 1150 van der A, R., Veefkind, J. P., Vlietinck, J., Yu, H., and Zehner, C.: Impact of Coronavirus  
 1151 Outbreak on NO<sub>2</sub> Pollution Assessed Using TROPOMI and OMI Observations, 47,  
 1152 e2020GL087978, 10.1029/2020gl087978, 2020.

1153 Bierman: Factorization methods for Discrete Sequential estimation, Academic Press, 1977.

1154 Binkowski, F. S. and Roselle, S. J.: Models-3 community multiscale air quality (CMAQ) model  
 1155 aerosol component - I. Model description, Journal of Geophysical Research-Atmospheres, 108,  
 1156 10.1029/2001jd001409, 2003.

1157 Brandhorst, N., Erdal, D., and Neuweiler, I.: Soil moisture prediction with the ensemble Kalman  
 1158 filter: Handling uncertainty of soil hydraulic parameters, Advances in Water Resources, 110,  
 1159 360-370, 2017.

1160 Bruhwiler, L. M. P., Michalak, A. M., Peters, W., Baker, D. F., and Tans, P.: An improved Kalman  
 1161 Smoother for atmospheric inversions, Atmos. Chem. Phys., 5, 2691-2702, 10.5194/acp-5-  
 1162 2691-2005, 2005.

1163 Carlton, A. G., Turpin, B. J., Altieri, K. E., Seitzinger, S. P., Mathur, R., Roselle, S. J., and Weber,  
 1164 R. J.: CMAQ Model Performance Enhanced When In-Cloud Secondary Organic Aerosol is  
 1165 Included: Comparisons of Organic Carbon Predictions with Measurements, Environmental  
 1166 Science & Technology, 42, 8798-8802, 2008

1167 Chen, D., Liu, Z., Ban, J., and Chen, M.: The 2015 and 2016 wintertime air pollution in China: SO<sub>2</sub>  
 1168 emission changes derived from a WRF-Chem/EnKF coupled data assimilation system,  
 1169 Atmospheric Chemistry and Physics, 19, 8619-8650, 10.5194/acp-19-8619-2019, 2019.

1170 Chen, D., Liu, Z., Fast, J., and Ban, J.: Simulations of sulfate-nitrate-ammonium (SNA) aerosols  
 1171 during the extreme haze events over northern China in October 2014, Atmospheric Chemistry  
 1172 and Physics, 16, 10707-10724, 10.5194/acp-16-10707-2016, 2016.

1173 Chevallier, F., Bréon, F.-M., and Rayner, P. J.: Contribution of the Orbiting Carbon Observatory to  
 1174 the estimation of CO<sub>2</sub> sources and sinks: Theoretical study in a variational data assimilation  
 1175 framework, 112, 10.1029/2006JD007375, 2007.

1176 Clements, A. L., Fraser, M. P., Upadhyay, N., Herckes, P., Sundblom, M., Lantz, J., and Solomon,  
 1177 P. A.: Chemical characterization of coarse particulate matter in the Desert Southwest - Pinal  
 1178 County Arizona, USA, Atmospheric Pollution Research, 5, 52-61, 10.5094/apr.2014.007, 2014.

1179 Clements, N., Hannigan, M. P., Miller, S. L., Peel, J. L., and Milford, J. B.: Comparisons of urban  
 1180 and rural PM<sub>10-2.5</sub> and PM<sub>2.5</sub> mass concentrations and semi-volatile fractions in northeastern  
 1181 Colorado, Atmospheric Chemistry and Physics, 16, 7469-7484, 10.5194/acp-16-7469-2016,  
 1182 2016.

1183 Daley, R.: Atmospheric Data Assimilation (gtSpecial Issue>Data Assimilation in Meteorology and  
 1184 Oceanography: Theory and Practice), Journal of the Meteorological Society of Japan. Ser. II,  
 1185 75, 319-329, 1997.

1186 Derber, J. C.: A VARIATIONAL CONTINUOUS ASSIMILATION TECHNIQUE, Monthly  
1187 Weather Review, 117, 2437-2446, 1989.

1188 de Foy, B., Lu, Z., Streets, D. G., Lamsal, L. N., and Duncan, B. N.: Estimates of power plant NOx  
1189 emissions and lifetimes from OMI NO2 satellite retrievals, Atmospheric Environment, 116, 1-  
1190 11, 10.1016/j.atmosenv.2015.05.056, 2015.

1191 De Lannoy, G. J. M., Houser, P. R., Pauwels, V. R. N., and Verhoest, N. E. C.: State and bias  
1192 estimation for soil moisture profiles by an ensemble Kalman filter: Effect of assimilation depth  
1193 and frequency, 43, 2007.

1194 Ding, J., van der A, R. J., Mijling, B., Levelt, P. F., and Hao, N.: NOx emission estimates during the  
1195 2014 Youth Olympic Games in Nanjing, Atmospheric Chemistry and Physics, 15, 9399-9412,  
1196 10.5194/acp-15-9399-2015, 2015.

1197 Elbern, H., Strunk, A., Schmidt, H., and Talagrand, O.: Emission rate and chemical state estimation  
1198 by 4-dimensional variational inversion, Atmospheric Chemistry and Physics, 7, 3749-3769,  
1199 10.5194/acp-7-3749-2007, 2007.

1200 Evensen, G.: The Ensemble Kalman Filter for Combined State and Parameter Estimation MONTE  
1201 CARLO TECHNIQUES FOR DATA ASSIMILATION IN LARGE SYSTEMS, Ieee Control  
1202 Systems Magazine, 29, 83-104, 10.1109/mcs.2009.932223, 2009.

1203 Feng, S., Jiang, F., Jiang, Z., Wang, H., Cai, Z., and Zhang, L.: Impact of 3DVAR assimilation of  
1204 surface PM2.5 observations on PM2.5 forecasts over China during wintertime, Atmospheric  
1205 Environment, 187, 34-49, 10.1016/j.atmosenv.2018.05.049, 2018.

1206 Feng, S., Jiang, F., Wang, H., Shen, Y., Zheng, Y., Zhang, L., Lou, C., and Ju, W.: Anthropogenic  
1207 emissions estimated using surface observations and their impacts on PM2.5 source  
1208 apportionment over the Yangtze River Delta, China, Science of The Total Environment, 828,  
1209 154522, 2022

1210 Feng, S., Jiang, F., Wu, Z., Wang, H., Ju, W., and Wang, H.: CO Emissions Inferred From Surface  
1211 CO Observations Over China in December 2013 and 2017, Journal of Geophysical Research-  
1212 Atmospheres, 125, 10.1029/2019jd031808, 2020a.

1213 Feng, S., Jiang, F., Wang, H., Wang, H., Ju, W., Shen, Y., Zheng, Y., Wu, Z., and Ding, A.: NOx  
1214 Emission Changes Over China During the COVID-19 Epidemic Inferred From Surface NO2  
1215 Observations, Geophysical Research Letters, 47, 10.1029/2020gl090080, 2020b.

1216 Feng, S. and Jiang, F.: Anthropogenic air pollutant emissions over China inferred by Regional multi-  
1217 Air Pollutant Assimilation System (RAPAS v1.0), Zenodo, 10.5281/zenodo.4718290, 2021.

1218 Gaspari, G. and Cohn, S. E.: Construction of correlation functions in two and three dimensions,  
1219 Quarterly Journal of the Royal Meteorological Society, 125, 723-757, 10.1256/smsqj.55416,  
1220 1999.

1221 Guenther, A. B., Jiang, X., Heald, C. L., Sakulyanontvittaya, T., Duhl, T., Emmons, L. K., and Wang,  
1222 X.: The Model of Emissions of Gases and Aerosols from Nature version 2.1 (MEGAN2.1): an  
1223 extended and updated framework for modeling biogenic emissions, Geoscientific Model



- 1224 Development, 5, 1471-1492, 10.5194/gmd-5-1471-2012, 2012.
- 1225 Gurney, K. R., Law, R. M., Denning, A. S., Rayner, P. J., Pak, B. C., Baker, D., Bousquet, P.,  
1226 Bruhwiler, L., Chen, Y. H., Ciais, P., Fung, I. Y., Heimann, M., John, J., Maki, T., Maksyutov,  
1227 S., Peylin, P., Prather, M., and Taguchi, S.: Transcom 3 inversion intercomparison: Model mean  
1228 results for the estimation of seasonal carbon sources and sinks, *Global Biogeochemical Cycles*,  
1229 18, 10.1029/2003gb002111, 2004.
- 1230 He, W., van der Velde, I. R., Andrews, A. E., Sweeney, C., Miller, J., Tans, P., van der Laan-Luijkx,  
1231 I. T., Nehr Korn, T., Mountain, M., Ju, W., Peters, W., and Chen, H.: CTDAS-Lagrange v1.0: a  
1232 high-resolution data assimilation system for regional carbon dioxide observations,  
1233 *Geoscientific Model Development*, 11, 3515-3536, 10.5194/gmd-11-3515-2018, 2018.
- 1234 Hinds, W.C.: *Aerosol Technology: Properties, Behavior, and Measurement of Airborne Particles*.  
1235 New York: John Wiley, 1982.
- 1236 Houtekamer, P. L. and Mitchell, H. L.: A sequential ensemble Kalman filter for atmospheric data  
1237 assimilation, *Monthly Weather Review*, 129, 123-137, 10.1175/1520-  
1238 0493(2001)129<0123:asekff>2.0.co;2, 2001.
- 1239 Houtekamer, P. L. and Zhang, F.: Review of the Ensemble Kalman Filter for Atmospheric Data  
1240 Assimilation, *Monthly Weather Review*, 144, 4489-4532, 10.1175/mwr-d-15-0440.1, 2016.
- 1241 Inness, A., Blechschmidt, A. M., Bouarar, I., Chabrilat, S., Crepulja, M., Engelen, R. J., Eskes, H.,  
1242 Flemming, J., Gaudel, A., Hendrick, F., Huijnen, V., Jones, L., Kapsomenakis, J., Katragkou,  
1243 E., Keppens, A., Langerock, B., de Maziere, M., Melas, D., Parrington, M., Peuch, V. H.,  
1244 Razinger, M., Richter, A., Schultz, M. G., Suttie, M., Thouret, V., Vrekoussis, M., Wagner, A.,  
1245 and Zerefos, C.: Data assimilation of satellite-retrieved ozone, carbon monoxide and nitrogen  
1246 dioxide with ECMWF's Composition-IFS, *Atmospheric Chemistry and Physics*, 15, 5275-5303,  
1247 2015.
- 1248 Jiang, F., Liu, Q., Huang, X., Wang, T., Zhuang, B., and Xie, M.: Regional modeling of secondary  
1249 organic aerosol over China using WRF/Chem, *Journal of Aerosol Science*, 43, 57-73,  
1250 10.1016/j.jaerosci.2011.09.003, 2012a.
- 1251 Jiang, F., Zhou, P., Liu, Q., Wang, T., Zhuang, B., and Wang, X.: Modeling tropospheric ozone  
1252 formation over East China in springtime, *Journal of Atmospheric Chemistry*, 69, 303-319,  
1253 10.1007/s10874-012-9244-3, 2012b.
- 1254 Jiang, F., Wang, H. M., Chen, J. M., Machida, T., Zhou, L. X., Ju, W. M., Matsueda, H., and Sawa,  
1255 Y.: Carbon balance of China constrained by CONTRAIL aircraft CO<sub>2</sub> measurements,  
1256 *Atmospheric Chemistry and Physics*, 14, 10133-10144, 10.5194/acp-14-10133-2014, 2014.
- 1257 Jiang, F., Wang, H., Chen, J. M., Ju, W., Tian, X., Feng, S., Li, G., Chen, Z., Zhang, S., Lu, X., Liu,  
1258 J., Wang, H., Wang, J., He, W., and Wu, M.: Regional CO<sub>2</sub> fluxes from 2010 to 2015 inferred  
1259 from GOSAT XCO<sub>2</sub> retrievals using a new version of the Global Carbon Assimilation System,  
1260 *Atmos. Chem. Phys.*, 21, 1963-1985, 10.5194/acp-21-1963-2021, 2021.
- 1261 Jiang, W., Smyth, S., Giroux, E., Roth, H., and Yin, D.: Differences between CMAQ fine mode  
1262 particle and PM<sub>2.5</sub> concentrations and their impact on model performance evaluation in the

1263 lower Fraser valley, *Atmospheric Environment*, 40, 4973-4985,  
1264 10.1016/j.atmosenv.2005.10.069, 2006.

1265 Jiang, Z., Jones, D. B. A., Worden, H. M., Deeter, M. N., Henze, D. K., Worden, J., Bowman, K. W.,  
1266 Brenninkmeijer, C. A. M., and Schuck, T. J.: Impact of model errors in convective transport on  
1267 CO source estimates inferred from MOPITT CO retrievals, *Journal Of Geophysical Research-*  
1268 *Atmospheres*, 118, 2073-2083, 2013a.

1269 Jiang, Z., Liu, Z., Wang, T., Schwartz, C. S., Lin, H.-C., and Jiang, F.: Probing into the impact of  
1270 3DVAR assimilation of surface PM10 observations over China using process analysis, *Journal*  
1271 *of Geophysical Research: Atmospheres*, 118, 6738-6749, 10.1002/jgrd.50495, 2013b.

1272 Jiang, Z., Worden, J. R., Worden, H., Deeter, M., Jones, D. B. A., Arellano, A. F., and Henze, D. K.:  
1273 A 15-year record of CO emissions constrained by MOPITT CO observations, *Atmospheric*  
1274 *Chemistry And Physics*, 17, 4565-4583, 10.5194/acp-17-4565-2017, 2017.

1275 Jin, J., Lin, H. X., Heemink, A., and Segers, A.: Spatially varying parameter estimation for dust  
1276 emissions using reduced-tangent-linearization 4DVar, *Atmospheric Environment*, 187, 358-  
1277 373, 10.1016/j.atmosenv.2018.05.060, 2018.

1278 Kahnert, M.: Variational data analysis of aerosol species in a regional CTM: background error  
1279 covariance constraint and aerosol optical observation operators, *Tellus B*, 60, 2008.

1280 Kang, J.-S., Kalnay, E., Miyoshi, T., Liu, J., and Fung, I.: Estimation of surface carbon fluxes with  
1281 an advanced data assimilation methodology, 117, 10.1029/2012JD018259, 2012.

1282 Keppenne, C. L., Rienecker, M. M., Kurkowski, N. P., and Adamec, D. A.: Ensemble Kalman filter  
1283 assimilation of temperature and altimeter data with bias correction and application to seasonal  
1284 prediction, *Nonlin. Processes Geophys.*, 12, 491-503, 2005.

1285 Kleist, D. T., Parrish, D. F., Derber, J. C., Treadon, R., Wu, W.-S., and Lord, S.: Introduction of the  
1286 GSI into the NCEP Global Data Assimilation System, *Weather and Forecasting*, 24, 1691-1705,  
1287 10.1175/2009waf2222201.1, 2009.

1288 Kong, L., Tang, X., Zhu, J., Wang, Z., Pan, Y., Wu, H., Wu, L., Wu, Q., He, Y., Tian, S., Xie, Y., Liu,  
1289 Z., Sui, W., Han, L., and Carmichael, G.: Improved Inversion of Monthly Ammonia Emissions  
1290 in China Based on the Chinese Ammonia Monitoring Network and Ensemble Kalman Filter,  
1291 *Environmental Science & Technology*, 53, 12529-12538, 10.1021/acsest.9b02701, 2019a.

1292 Kong, L., Tang, X., Zhu, J., Wang, Z., Fu, J. S., Wang, X., Itahashi, S., Yamaji, K., Nagashima, T.,  
1293 Lee, H. J., Kim, C. H., Lin, C. Y., Chen, L., Zhang, M., Tao, Z., Li, J., Kajino, M., Liao, H.,  
1294 Sudo, K., Wang, Y., Pan, Y., Tang, G., Li, M., Wu, Q., Ge, B., and Carmichael, G. R.: Evaluation  
1295 and uncertainty investigation of the NO<sub>2</sub>, CO and NH<sub>3</sub> modeling over China under the  
1296 framework of MICS-Asia III, *Atmos. Chem. Phys. Discuss.*, 2019, 1-33, 10.5194/acp-2018-  
1297 1158, 2019b.

1298 Laloyaux, P., Bonavita, M., Chrust, M., and Gürol, S.: Exploring the potential and limitations of  
1299 weak-constraint 4D-Var, *Quarterly Journal of the Royal Meteorological Society*, 146, 4067-  
1300 4082, 2020

1301 Li, J.-d., Deng, Q.-h., Lu, C., and Huang, B.-l.: Chemical compositions and source apportionment  
1302 of atmospheric PM10 in suburban area of Changsha, China, *Journal of Central South*  
1303 *University of Technology*, 17, 509-515, 2010.

1304 Li, M., Zhang, Q., Kurokawa, J.-i., Woo, J.-H., He, K., Lu, Z., Ohara, T., Song, Y., Streets, D. G.,  
1305 Carmichael, G. R., Cheng, Y., Hong, C., Huo, H., Jiang, X., Kang, S., Liu, F., Su, H., and Zheng,  
1306 B.: MIX: a mosaic Asian anthropogenic emission inventory under the international  
1307 collaboration framework of the MICS-Asia and HTAP, *Atmospheric Chemistry and Physics*,  
1308 17, 935-963, 10.5194/acp-17-935-2017, 2017.

1309 Liu, C. and Shi, K.: A review on methodology in O3-NOx-VOC sensitivity study, *Environmental*  
1310 *Pollution*, 291, 118249, 2021.

1311 Liu, Y., Kalnay, E., Zeng, N., Asrar, G., Chen, Z., and Jia, B.: Estimating surface carbon fluxes based  
1312 on a local ensemble transform Kalman filter with a short assimilation window and a long  
1313 observation window: an observing system simulation experiment test in GEOS-Chem 10.1,  
1314 *Geoscientific Model Development*, 12, 2899-2914, 2019.

1315 Liu, Z., Liu, Q., Lin, H.-C., Schwartz, C. S., Lee, Y.-H., and Wang, T.: Three-dimensional variational  
1316 assimilation of MODIS aerosol optical depth: Implementation and application to a dust storm  
1317 over East Asia, *Journal of Geophysical Research: Atmospheres*, 116, n/a-n/a,  
1318 10.1029/2011jd016159, 2011.

1319 Lorenc, A. C.: Modelling of error covariances by 4D-Var data assimilation, *Quarterly Journal of the*  
1320 *Royal Meteorological Society*, 129, 3167-3182, 2003.

1321 Hamer, P. D., Bowman, K. W., Henze, D. K., Attie, J. L., and Marecal, V.: The impact of observing  
1322 characteristics on the ability to predict ozone under varying polluted photochemical regimes,  
1323 *Atmospheric Chemistry and Physics*, 15, 10645-10667, 2015.

1324 Ma, C., Wang, T., Mizzi, A. P., Anderson, J. L., Zhuang, B., Xie, M., and Wu, R.: Multiconstituent  
1325 Data Assimilation With WRF-Chem/DART: Potential for Adjusting Anthropogenic Emissions  
1326 and Improving Air Quality Forecasts Over Eastern China, 124, 7393-7412,  
1327 10.1029/2019jd030421, 2019.

1328 Meirink, J. F., Bergamaschi, P., and Krol, M. C.: Four-dimensional variational data assimilation for  
1329 inverse modelling of atmospheric methane emissions: method and comparison with synthesis  
1330 inversion, *Atmospheric Chemistry and Physics*, 8, 6341-6353, 2008.

1331 Meirink, J. F., Eskes, H. J., and Goede, A. P. H.: Sensitivity analysis of methane emissions derived  
1332 from SCIAMACHY observations through inverse modelling, *Atmospheric Chemistry and*  
1333 *Physics*, 6, 1275-1292, 10.5194/acp-6-1275-2006, 2006.

1334 Maybeck: *Stochastic Models, Estimation and Control* Academic Press, 1979.

1335 Miyazaki, K. and Eskes, H.: Constraints on surface NOx emissions by assimilating satellite  
1336 observations of multiple species, *Geophysical Research Letters*, 40, 4745-4750,  
1337 10.1002/grl.50894, 2013.

1338 Miyazaki, K., Eskes, H. J., and Sudo, K.: Global NOx emission estimates derived from an

1339 assimilation of OMI tropospheric NO<sub>2</sub> columns, *Atmospheric Chemistry and Physics*, 12,  
1340 2263-2288, 10.5194/acp-12-2263-2012, 2012a.

1341 Miyazaki, K., Eskes, H. J., Sudo, K., Takigawa, M., van Weele, M., and Boersma, K. F.:  
1342 Simultaneous assimilation of satellite NO<sub>2</sub>, O<sub>3</sub>, CO, and HNO<sub>3</sub> data for the analysis of  
1343 tropospheric chemical composition and emissions, *Atmospheric Chemistry and Physics*, 12,  
1344 9545-9579, 10.5194/acp-12-9545-2012, 2012b.

1345 Miyazaki, K., Eskes, H., Sudo, K., Boersma, K. F., Bowman, K., and Kanaya, Y.: Decadal changes  
1346 in global surface NO<sub>x</sub> emissions from multi-constituent satellite data assimilation,  
1347 *Atmospheric Chemistry and Physics*, 17, 807-837, 2017.

1348 Mizzi, A. P., Edwards, D. P., and Anderson, J. L.: Assimilating compact phase space retrievals  
1349 (CPSRs): comparison with independent observations (MOZAIC in situ and IASI retrievals)  
1350 and extension to assimilation of truncated retrieval profiles, *Geoscientific Model Development*,  
1351 11, 3727-3745, 2018.

1352 Monteil, G., Houweling, S., Butz, A., Guerlet, S., Schepers, D., Hasekamp, O., Frankenberg, C.,  
1353 Scheepmaker, R., Aben, I., and Rockmann, T.: Comparison of CH<sub>4</sub> inversions based on 15  
1354 months of GOSAT and SCIAMACHY observations, *Journal of Geophysical Research-*  
1355 *Atmospheres*, 118, 11807-11823, 2013.

1356 Muller, J. F. and Stavrou, T.: Inversion of CO and NO<sub>x</sub> emissions using the adjoint of the  
1357 IMAGES model, *Atmospheric Chemistry and Physics*, 5, 1157-1186, 2005.

1358 Nassar, R., Jones, D. B. A., Kulawik, S. S., Worden, J. R., Bowman, K. W., Andres, R. J.,  
1359 Suntharalingam, P., Chen, J. M., Brenninkmeijer, C. A. M., Schuck, T. J., Conway, T. J., and  
1360 Worthy, D. E.: Inverse modeling of CO<sub>2</sub> sources and sinks using satellite observations of CO<sub>2</sub>  
1361 from TES and surface flask measurements, *Atmospheric Chemistry and Physics*, 11, 6029-  
1362 6047, 2011.

1363 Navon, I. M.: Practical and theoretical aspects of adjoint parameter estimation and identifiability in  
1364 meteorology and oceanography, *Dynamics of Atmospheres and Oceans*, 27, 55-79, 1998.

1365 Parrish, D. F. and Derber, J. C.: The National Meteorological Center's spectral statistical-  
1366 interpolation analysis system, *Monthly Weather Review*, 120, 1747-1763, 10.1175/1520-  
1367 0493(1992)120<1747:tnmc>2.0.co;2, 1992.

1368 Paulot, F., Jacob, D. J., Pinder, R. W., Bash, J. O., Travis, K., and Henze, D. K.: Ammonia emissions  
1369 in the United States, European Union, and China derived by high-resolution inversion of  
1370 ammonium wet deposition data: Interpretation with a new agricultural emissions inventory  
1371 (MASAGE\_NH<sub>3</sub>), *Journal of Geophysical Research-Atmospheres*, 119, 4343-4364, 2014.

1372 Peng, Z., Liu, Z., Chen, D., and Ban, J.: Improving PM<sub>2.5</sub> forecast over  
1373 China by the joint adjustment of initial conditions and source emissions with an ensemble  
1374 Kalman filter, *Atmospheric Chemistry and Physics*, 17, 4837-4855, 10.5194/acp-17-4837-  
1375 2017, 2017.

1376 Peng, Z., Lei, L., Liu, Z., Su, J., Ding, A., Ban, J., Chen, D., Kou, X., and Chu, K.: The impact of  
1377 multi-species surface chemical observation assimilation on air quality forecasts in China,

- 1378 Atmospheric Chemistry and Physics, 18, 10.5194/acp-18-17387-2018, 2018.
- 1379 Peters, W., Jacobson, A. R., Sweeney, C., Andrews, A. E., Conway, T. J., Masarie, K., Miller, J. B.,  
1380 Bruhwiler, L. M. P., Petron, G., Hirsch, A. I., Worthy, D. E. J., van der Werf, G. R., Randerson,  
1381 J. T., Wennberg, P. O., Krol, M. C., and Tans, P. P.: An atmospheric perspective on North  
1382 American carbon dioxide exchange: CarbonTracker, Proceedings of the National Academy of  
1383 Sciences of the United States of America, 104, 18925-18930, 10.1073/pnas.0708986104, 2007.
- 1384 Peylin, P., Rayner, P. J., Bousquet, P., Carouge, C., Hourdin, F., Heinrich, P., Ciais, P., and  
1385 contributors, A.: Daily CO<sub>2</sub> flux estimates over Europe from continuous atmospheric  
1386 measurements: 1, inverse methodology, Atmospheric Chemistry and Physics, 5, 3173-3186,  
1387 10.5194/acp-5-3173-2005, 2005.
- 1388 Purser, R. J., Wu, W. S., Parrish, D. F., and Roberts, N. M.: Numerical aspects of the application of  
1389 recursive filters to variational statistical analysis. Part I: Spatially homogeneous and isotropic  
1390 Gaussian covariances, Monthly Weather Review, 131, 1524-1535, 10.1175//1520-  
1391 0493(2003)131<1524:naotao>2.0.co;2, 2003.
- 1392 Quan, J., Liu, Q., Li, X., Gao, Y., Jia, X., Sheng, J., Liu, Y., 2015. Effect of heterogeneous aqueous  
1393 reactions on the secondary formation of inorganic aerosols during haze events. Atmospheric  
1394 Environment 122, 306-312.
- 1395 Rabier, F., McNally, A., Andersson, E., Courtier, P., Uden, P., Eyre, J., Hollingsworth, A., and  
1396 Bouttier, F.: The ECMWF implementation of three-dimensional variational assimilation (3D-  
1397 Var). II: Structure functions, Quarterly Journal Of the Royal Meteorological Society, 124,  
1398 1809-1829, 10.1256/smsqj.55002, 1998.
- 1399 Reichle, R. H., McLaughlin, D. B., and Entekhabi, D.: Hydrologic data assimilation with the  
1400 ensemble Kalman filter, Monthly Weather Review, 130, 103-114, 2002.
- 1401 Richardson, H., Basu, S., and Holtslag, A. A. M.: Improving Stable Boundary-Layer Height  
1402 Estimation Using a Stability-Dependent Critical Bulk Richardson Number, Boundary-Layer  
1403 Meteorology, 148, 93-109, 2013.
- 1404 Ruiz, J. and Pulido, M.: Parameter Estimation Using Ensemble-Based Data Assimilation in the  
1405 Presence of Model Error, Monthly Weather Review, 143, 1568-1582, 2015.
- 1406 Sarwar, G., Simon, H., Bhave, P., and Yarwood, G.: Examining the impact of heterogeneous nitril  
1407 chloride production on air quality across the United States, Atmospheric Chemistry and  
1408 Physics, 12, 6455-6473, 10.5194/acp-12-6455-2012, 2012.
- 1409 Sasaki, Y.: SOME BASIC FORMALISMS IN NUMERICAL VARIATIONAL ANALYSIS,  
1410 Monthly Weather Review, 98, 875-&, 1970.
- 1411 Schneising, O., Buchwitz, M., Burrows, J. P., Bovensmann, H., Bergamaschi, P., and Peters, W.:  
1412 Three years of greenhouse gas column-averaged dry air mole fractions retrieved from satellite  
1413 - Part 2: Methane, Atmospheric Chemistry and Physics, 9, 443-465, 2009.
- 1414 Schwartz, C. S., Liu, Z., Lin, H.-C., and Cetola, J. D.: Assimilating aerosol observations with a  
1415 "hybrid" variational-ensemble data assimilation system, Journal Of Geophysical Research-

- 1416 Atmospheres, 119, 4043-4069, 10.1002/2013jd020937, 2014.
- 1417 Sekiyama, T. T., Tanaka, T. Y., Shimizu, A., and Miyoshi, T.: Data assimilation of CALIPSO aerosol  
1418 observations, *Atmospheric Chemistry and Physics*, 10, 39-49, 10.5194/acp-10-39-2010, 2010.
- 1419 Shen, Y., Jiang, F., Feng, S., Zheng, Y., Cai, Z., and Lyu, X.: Impact of weather and emission changes  
1420 on NO<sub>2</sub> concentrations in China during 2014–2019, *Environmental Pollution*, 269, 116163,  
1421 10.1016/j.envpol.2020.116163, 2021.
- 1422 Shi, X. and Brasseur, G. P.: The Response in Air Quality to the Reduction of Chinese Economic  
1423 Activities During the COVID-19 Outbreak, 47, e2020GL088070, 10.1029/2020gl088070,  
1424 2020.
- 1425 Stanevich, I., Jones, D. B. A., Strong, K., Keller, M., Henze, D. K., Parker, R. J., Boesch, H., Wunch,  
1426 D., Notholt, J., Petri, C., Warneke, T., Sussmann, R., Schneider, M., Hase, F., Kivi, R.,  
1427 Deutscher, N. M., Velazco, V. A., Walker, K. A., and Deng, F.: Characterizing model errors in  
1428 chemical transport modeling of methane: using GOSAT XCH<sub>4</sub> data with weak-constraint four-  
1429 dimensional variational data assimilation, *Atmospheric Chemistry and Physics*, 21, 9545-9572,  
1430 2021.
- 1431 Stavrakou, T., Müller, J.-F., Boersma, K. F., De Smedt, I., and van der A, R. J.: Assessing the  
1432 distribution and growth rates of NO<sub>x</sub> emission sources by inverting a 10-year record of NO<sub>2</sub>  
1433 satellite columns, 35, 10.1029/2008gl033521, 2008.
- 1434 Sun, A. Y., Morris, A., and Mohanty, S.: Comparison of deterministic ensemble Kalman filters for  
1435 assimilating hydrogeological data, *Advances in Water Resources*, 32, 280-292,  
1436 10.1016/j.advwatres.2008.11.006, 2009.
- 1437 Takagi, H., Saeki, T., Oda, T., Saito, M., Valsala, V., Belikov, D., Saito, R., Yoshida, Y., Morino, I.,  
1438 Uchino, O., Andres, R. J., Yokota, T., and Maksyutov, S.: On the Benefit of GOSAT  
1439 Observations to the Estimation of Regional CO<sub>2</sub> Fluxes, *SOLA*, 7, 161-164,  
1440 10.2151/sola.2011-041, 2011.
- 1441 Tang, X., Zhu, J., Wang, Z. F., and Gbaguidi, A.: Improvement of ozone forecast over Beijing based  
1442 on ensemble Kalman filter with simultaneous adjustment of initial conditions and emissions,  
1443 *Atmospheric Chemistry And Physics*, 11, 12901-12916, 10.5194/acp-11-12901-2011, 2011.
- 1444 Tang, X., Zhu, J., Wang, Z. F., Wang, M., Gbaguidi, A., Li, J., Shao, M., Tang, G. Q., and Ji, D. S.:  
1445 Inversion of CO emissions over Beijing and its surrounding areas with ensemble Kalman filter,  
1446 *Atmospheric Environment*, 81, 676-686, 10.1016/j.atmosenv.2013.08.051, 2013.
- 1447 Wang, C., Lei, L., Tan, Z.-M., and Chu, K.: Adaptive Localization for Tropical Cyclones With  
1448 Satellite Radiances in an Ensemble Kalman Filter, *Frontiers in Earth Science*, 8,  
1449 10.3389/feart.2020.00039, 2020.
- 1450 Wang, H., Jiang, F., Wang, J., Ju, W., and Chen, J. M.: Terrestrial ecosystem carbon flux estimated  
1451 using GOSAT and OCO-2 XCO<sub>2</sub> retrievals, *Atmospheric Chemistry and Physics*, 19, 12067-  
1452 12082, 2019a.
- 1453 Wang, N., Lyu, X., Deng, X., Huang, X., Jiang, F., and Ding, A.: Aggravating O<sub>3</sub> pollution due to

- 1454 NOx emission control in eastern China, *Science of The Total Environment*, 677, 732-744,  
1455 2019b.
- 1456 Wang, Y. H., Hu, B., Ji, D. S., Liu, Z. R., Tang, G. Q., Xin, J. Y., Zhang, H. X., Song, T., Wang, L.  
1457 L., Gao, W. K., Wang, X. K., and Wang, Y. S.: Ozone weekend effects in the Beijing-Tianjin-  
1458 Hebei metropolitan area, China, *Atmospheric Chemistry and Physics*, 14, 2419-2429, 2014.
- 1459 Wang, Z., Li, Y., Dong, X., Sun, R., Sun, N., and Pan, L.: Analysis on weekend effect of air  
1460 pollutants in urban atmosphere of Beijing, *Journal of University of Chinese Academy of  
1461 Sciences*, 32, 843-850, 2015.
- 1462 Wang, Z., Wang, W., Tham, Y.J., Li, Q., Wang, H., Wen, L., Wang, X., Wang, T., 2017. Fast  
1463 heterogeneous N<sub>2</sub>O<sub>5</sub> uptake and ClNO<sub>2</sub> production in power plant and industrial plumes  
1464 observed in the nocturnal residual layer over the North China Plain. *Atmospheric Chemistry  
1465 and Physics* 17, 12361-12378.
- 1466 Wecht, K. J., Jacob, D. J., Sulprizio, M. P., Santoni, G. W., Wofsy, S. C., Parker, R., Boesch, H., and  
1467 Worden, J.: Spatially resolving methane emissions in California: constraints from the CalNex  
1468 aircraft campaign and from present (GOSAT, TES) and future (TROPOMI, geostationary)  
1469 satellite observations, *Atmospheric Chemistry and Physics*, 14, 8173-8184, 2014.
- 1470 Wu, H., Tang, X., Wang, Z., Wu, L., Li, J., Wang, W., Yang, W., and Zhu, J.: High-spatiotemporal-  
1471 resolution inverse estimation of CO and NO<sub>x</sub> emission reductions during emission control  
1472 periods with a modified ensemble Kalman filter, *Atmospheric Environment*, 236,  
1473 10.1016/j.atmosenv.2020.117631, 2020.
- 1474 Wu, W. S., Purser, R. J., and Parrish, D. F.: Three-dimensional variational analysis with spatially  
1475 inhomogeneous covariances, *Monthly Weather Review*, 130, 2905-2916, 10.1175/1520-  
1476 0493(2002)130<2905:tdvaws>2.0.co;2, 2002.
- 1477 Yang, W., Li, J., Wang, W., Li, J., Ge, M., Sun, Y., Chen, X., Ge, B., Tong, S., Wang, Q., and Wang,  
1478 Z.: Investigating secondary organic aerosol formation pathways in China during 2014,  
1479 *Atmospheric Environment*, 213, 133-147, 2019.
- 1480 Yumimoto, K., Uno, I., Sugimoto, N., Shimizu, A., Liu, Z., and Winker, D. M.: Adjoint inversion  
1481 modeling of Asian dust emission using lidar observations, *Atmospheric Chemistry and Physics*,  
1482 8, 2869-2884, 2008.
- 1483 Zhang, F., Weng, Y., Sippel, J. A., Meng, Z., and Bishop, C. H.: Cloud-Resolving Hurricane  
1484 Initialization and Prediction through Assimilation of Doppler Radar Observations with an  
1485 Ensemble Kalman Filter, *Monthly Weather Review*, 137, 2105-2125, 10.1175/2009mwr2645.1,  
1486 2009a.
- 1487 Zhang, L., Chen, Y., Zhao, Y., Henze, D. K., Zhu, L., Song, Y., Paulot, F., Liu, X., Pan, Y., Lin, Y.,  
1488 and Huang, B.: Agricultural ammonia emissions in China: reconciling bottom-up and top-down  
1489 estimates, *Atmospheric Chemistry and Physics*, 18, 339-355, 2018.
- 1490 Zhang, Q., Streets, D. G., Carmichael, G. R., He, K. B., Huo, H., Kannari, A., Klimont, Z., Park, I.  
1491 S., Reddy, S., Fu, J. S., Chen, D., Duan, L., Lei, Y., Wang, L. T., and Yao, Z. L.: Asian emissions  
1492 in 2006 for the NASA INTEX-B mission, *Atmospheric Chemistry and Physics*, 9, 5131-5153,

- 1493 10.5194/acp-9-5131-2009, 2009b.
- 1494 Zhang, S., Zheng, X., Chen, J. M., Chen, Z., Dan, B., Yi, X., Wang, L., and Wu, G.: A global carbon  
1495 assimilation system using a modified ensemble Kalman filter, *Geosci. Model Dev.*, 8, 805-816,  
1496 10.5194/gmd-8-805-2015, 2015.
- 1497 Zhang, X., Liu, J., Han, H., Zhang, Y., Jiang, Z., Wang, H., Meng, L., Li, Y. C., and Liu, Y.: Satellite-  
1498 Observed Variations and Trends in Carbon Monoxide over Asia and Their Sensitivities to  
1499 Biomass Burning, *Remote Sensing*, 12, 10.3390/rs12050830, 2020.
- 1500 Zheng, B., Tong, D., Li, M., Liu, F., Hong, C., Geng, G., Li, H., Li, X., Peng, L., Qi, J., Yan, L.,  
1501 Zhang, Y., Zhao, H., Zheng, Y., He, K., and Zhang, Q.: Trends in China's anthropogenic  
1502 emissions since 2010 as the consequence of clean air actions, *Atmospheric Chemistry And  
1503 Physics*, 18, 14095-14111, 10.5194/acp-18-14095-2018, 2018.
- 1504 Zheng, B., Zhang, Q., Tong, D., Chen, C., Hong, C., Li, M., Geng, G., Lei, Y., Huo, H., and He, K.:  
1505 Resolution dependence of uncertainties in gridded emission inventories: a case study in Hebei,  
1506 China, *Atmospheric Chemistry and Physics*, 17, 921-933, 2017.